




















<b>Publication Year</b>	2023
<b>Acceptance in OA @INAF</b>	2023-08-29T13:19:24Z
<b>Title</b>	A catalogue of radio supernova remnants and candidate supernova remnants in the EMU/POSSUM Galactic pilot field
<b>Authors</b>	Ball, Brianna D.; Kothes, Roland; Rosolowsky, Erik; West, Jennifer; Becker, Werner; et al.
<b>DOI</b>	10.1093/mnras/stad1953
<b>Handle</b>	<a href="http://hdl.handle.net/20.500.12386/34360">http://hdl.handle.net/20.500.12386/34360</a>
<b>Journal</b>	MONTHLY NOTICES OF THE ROYAL ASTRONOMICAL SOCIETY
<b>Number</b>	524

# A catalogue of radio supernova remnants and candidate supernova remnants in the EMU/POSSUM Galactic pilot field

Brianna D. Ball <sup>1,★</sup>, Roland Kothes,<sup>1</sup> Erik Rosolowsky <sup>1</sup>, Jennifer West <sup>2,3</sup>, Werner Becker <sup>4,5</sup>,  
Miroslav D. Filipović <sup>6</sup>, B.M. Gaensler <sup>3</sup>, Andrew M. Hopkins <sup>7</sup>, Bärbel Koribalski <sup>6,8</sup>,  
Tom Landecker <sup>2</sup>, Denis Leahy <sup>9</sup>, Joshua Marvil <sup>10</sup>, Xiaohui Sun <sup>11</sup>, Filomena Bufano <sup>12</sup>,  
Ettore Carretti <sup>13</sup>, Adriano Ingallinera <sup>12</sup>, Cameron L. Van Eck <sup>14</sup> and Tony Willis <sup>2</sup>

<sup>1</sup>Department of Physics, University of Alberta, 4-181 CCIS, Edmonton, Alberta T6G 2E1, Canada

<sup>2</sup>Dominion Radio Astrophysical Observatory, Herzberg Astronomy and Astrophysics, National Research Council Canada, P.O. Box 248, Penticon, BC V2A 6J9, Canada

<sup>3</sup>Dunlap Institute for Astronomy and Astrophysics, University of Toronto, 60 St. George Street, Toronto M5S 3H4, Canada

<sup>4</sup>Max-Planck-Institut für Extraterrestrische Physik, Gießenbachstraße 1, 85748 Garching, Germany

<sup>5</sup>Max-Planck-Institut für Radioastronomie, Auf dem Hügel 69, 53121 Bonn, Germany

<sup>6</sup>Physical Sciences, Western Sydney University, Locked Bag 1797, Penrith South DC, Sydney, NSW 1797, Australia

<sup>7</sup>Australian Astronomical Optics, Macquarie University, 105 Delhi Rd, North Ryde, NSW 2113, Australia

<sup>8</sup>Australia Telescope National Facility, CSIRO Astronomy and Space Science, P.O. Box 76, NSW 1710, NSW 1710, Epping, Australia

<sup>9</sup>Department of Physics and Astronomy, University of Calgary, 2500 University Drive NW, Calgary, AB T2N 1N4, Canada

<sup>10</sup>National Radio Astronomy Observatory, 1003 Lopezville Road, P.O. Box O, Socorro, NM 87801, USA

<sup>11</sup>School of Physics and Astronomy, Yunnan University, Kunming 650500, PR China

<sup>12</sup>INAF – Osservatorio Astrofisico di Catania, Via Santa Sofia, 78, 95123 Catania, Italy

<sup>13</sup>INAF, Istituto di Radioastronomia, Via Gobetti 101, 40129 Bologna, Italy

<sup>14</sup>Research School of Astronomy and Astrophysics, The Australian National University, Canberra ACT 2611, Australia

Accepted 2023 June 27. Received 2023 June 23; in original form 2023 May 10

## ABSTRACT

We use data from the pilot observations of the EMU/POSSUM surveys to study the ‘missing supernova remnant (SNR) problem’, the discrepancy between the number of Galactic SNRs that have been observed, and the number that are estimated to exist. The Evolutionary Map of the Universe (EMU) and the Polarization Sky Survey of the Universe’s Magnetism (POSSUM) are radio sky surveys that are conducted using the Australian Square Kilometre Array Pathfinder (ASKAP). We report on the properties of seven known SNRs in the joint Galactic pilot field, with an approximate longitude and latitude of  $323^\circ \leq l \leq 330^\circ$  and  $-4^\circ \leq b \leq 2^\circ$ , respectively, and identify 21 SNR candidates. Of these, four have been previously identified as SNR candidates, three were previously listed as a single SNR, 13 have not been previously studied, and one has been studied in the infrared. These are the first discoveries of Galactic SNR candidates with EMU/POSSUM and, if confirmed, they will increase the SNR density in this field by a factor of 4. By comparing our SNR candidates to the known Galactic SNR population, we demonstrate that many of these sources were likely missed in previous surveys due to their small angular size and/or low surface brightness. We suspect that there are SNRs in this field that remain undetected due to limitations set by the local background and confusion with other radio sources. The results of this paper demonstrate the potential of the full EMU/POSSUM surveys to uncover more of the missing Galactic SNR population.

**Key words:** catalogues – ISM: supernova remnants – Galaxy: general – radio continuum: general.

## 1 INTRODUCTION

Supernovae and supernova remnants (SNRs) are the most significant sources of chemical enrichment in the interstellar medium (ISM) of our Galaxy. More than half of the material in the Milky Way has been processed by supernovae and their remnants (Padmanabhan 2001). Thus, our knowledge of the Galaxy and its evolution is necessarily informed by our understanding of the Galactic SNR population.

In this paper, we seek to investigate the so-called ‘missing supernova remnant problem’, which refers to the discrepancy between the number of SNRs that are believed to exist in our Galaxy and the number that have been discovered (Brogan et al. 2006; Helfand et al. 2006; Green, Reeves & Murphy 2014; Green 2015). The exact size of the discrepancy is unknown, as accurately quantifying this problem is challenging due to variations in SNR density and radio visibility across the Galactic plane. Based on observations of extra-galactic supernovae, we know that in galaxies like ours a supernova should occur every 30–50 yr (Tammann, Loeffler & Schroeder 1994). We can combine this rate with the expected SNR radio lifetime to obtain

\* E-mail: [bdball@ualberta.ca](mailto:bdball@ualberta.ca)

an estimate of the number of SNRs that should be detectable at radio wavelengths.

The radio-visible lifetime of a SNR is difficult to estimate, however, as it likely varies based on local conditions and depends on the frequency of the observations. By studying associations between SNRs and pulsars, Frail, Goss & Whiteoak (1994) estimated the mean radio SNR lifetime to be about 60 000 yr. More recent work has shown that the majority of observed remnants in the Milky Way and Local Group galaxies are believed to be in the Sedov–Taylor (S–T) phase of evolution (Albert & Dwarkadas 2022). Thus, in many cases the S–T lifetime may serve as a useful proxy for the radio visible lifetime with a characteristic time-scale of 20–80 kyrs dependent on the local ISM density (Sarbadhicary et al. 2017). However, adopting these age limits may result in estimates which are too conservative. Around 25 per cent of known Galactic SNRs with age estimates are believed to be older than 20 kyrs (Ferrand & Safi-Harb 2012). Additionally, there have been discoveries of Galactic SNRs, observable at radio wavelengths, that are well beyond the S–T phase (Kothes et al. 2017). In comparing the Sarbadhicary et al. (2017) model predictions to observations, Leahy, Merrick & Filipović (2022) found the model to be insufficient in reproducing observed radio emission.

According to Ranasinghe & Leahy (2022), predictions for the total number of SNRs in the Galaxy should generally be  $>1000$ , so we adopt this as a lower limit. We form a conservative upper limit based on the supernova rate and S–T lifetime and estimate that at any given time, 1000–2700 radio SNRs should be detectable in our Galaxy. So far we have only discovered somewhere in the range of 300–400 (Ferrand & Safi-Harb 2012; Green 2022). We aim to detect some of these missing SNRs and, by studying their properties, gain further insight into the nature of this discrepancy.

The majority of SNRs (approximately 95 per cent) discovered in our Galaxy have been detected in the radio (Dubner 2017). Thus, radio observations play an important role in the search for Galactic SNRs. Because of the limitations in working with radio data due to the relatively poor angular resolution and sensitivity when compared to observations at shorter wavelengths, sources with a small angular size and/or low surface brightness are more likely to be missed. It is therefore reasonable to expect that these types of sources may comprise a significant portion of the missing SNR population. This is especially true in regions of the Galaxy where radio emission is dominated by thermal sources, such as H II regions, and distinguishing SNRs becomes more difficult. X-ray observations of young Galactic SNRs are believed to be fairly complete with an implied Galactic SNR birth rate of  $\sim 1/35$  yr, consistent with the supernova explosion rate (Leahy, Ranasinghe & Gelowitz 2020). Thus, we mostly expect to find old, faint SNRs of varying angular sizes, dependent on the distance to the source and the local environment.

Confusion with other extended radio sources, particularly H II regions, presents a significant challenge to confidently identifying SNR candidates. To address this, we adapt a commonly used methodology involving the comparison of radio and mid-infrared (MIR) fluxes. This technique has been used by many other Galactic SNR surveys, as well as in follow up studies of SNR candidates (Whiteoak & Green 1996; Brogan et al. 2006; Helfand et al. 2006; Green et al. 2014; Anderson et al. 2017; Hurley-Walker et al. 2019; Dokara et al. 2021). While SNRs and H II regions can have similar radio morphologies, H II regions produce strong MIR emission from warm dust and polycyclic aromatic hydrocarbons (PAHs). Conversely, SNRs have been found to produce little to no MIR emission (Fuerst, Reich & Sofue 1987; Whiteoak & Green 1996;

Pinheiro Gonçalves et al. 2011). The absence of an MIR counterpart can therefore be used as evidence that a potential SNR candidate is not an H II region.

The Evolutionary Map of the Universe (EMU) and the Polarization Sky Survey of the Universe’s Magnetism (POSSUM) are radio surveys that will be observed together with the Australian Square Kilometre Array Pathfinder (ASKAP). Because of the improved resolution and sensitivity when compared to previous southern sky radio surveys, such as the MGPS-2 (Green et al. 2014), the EMU/POSSUM surveys should be expected to uncover some of these small and faint sources. Additionally, ASKAP’s large field of view and good UV-coverage should allow for the detection of old SNRs that are large with low surface brightness. Here, we utilize data from the pilot observations of these surveys to search for SNRs within a small field of the Galactic plane.

In this paper, we aim to (1) validate the quality of the EMU/POSSUM Galactic pilot field data by studying the properties of known SNRs in the field, (2) identify new SNR candidates and uncover some of the missing SNR population, and (3) develop analysis techniques that can be used to study SNRs and search for new candidates with the full EMU/POSSUM sky survey data as they become available. Descriptions of the data used in this paper can be found in Section 2. In Section 3, we present the data and describe how SNR candidates were identified. We also discuss the known SNRs in the field and their properties. In Section 4, we present our SNR candidates and in Section 5 we provide some analysis and comparison to the known Galactic SNR population. The conclusions are summarized in Section 6.

## 2 METHODS AND OBSERVATIONS

### 2.1 The EMU and POSSUM observations with ASKAP

We use data from the ASKAP telescope (Hotan et al. 2021), an interferometer with 36 12-m dishes equipped with phased-array feeds (PAFs). These data were obtained during the commissioning phase of the telescope, specifically from the second pilot observations of the commensal EMU (Norris et al. 2011, 2021) and POSSUM surveys (Gaensler et al. 2010; Gaensler in preparation). These observations use a full 10-h track having full Stokes with 288 MHz bandwidth, centred at 933 MHz. Imaging is performed using ASKAPsoft and the standard commensal EMU/POSSUM imaging parameter set (Norris et al. 2021), which produces both a multifrequency synthesis (MFS) band-averaged Stokes I image for the EMU survey, and full Stokes I, Q, U, and V frequency cubes with 1 MHz channels for POSSUM. The cubes have been convolved to a common resolution of 18” across all PAF beams and all frequency channels. The observations for this particular pilot II survey field were observed on 2021 November 6 (Scheduling block 33284). Primary beam correction in all Stokes parameters are performed using beam models derived from standard observatory holography observations from 2021 June 20 (Scheduling block 28162). The long period of time between the holography and the observations resulted in a poor leakage correction, and therefore this field was re-observed on 2022 September 7 (SB 43773). This field was corrected using holography observations from 2022 July 28 (SB 43057). This improved correction mitigates leakage from Stokes I into Stokes Q and U at around the 1 per cent level or less over most of the field. The top image in Fig. 1 shows the Stokes I image from the original pilot II observation and the bottom image shows the same field in polarized intensity (PI). The PI was taken from the peak of the Faraday depth (FD) function for each pixel.



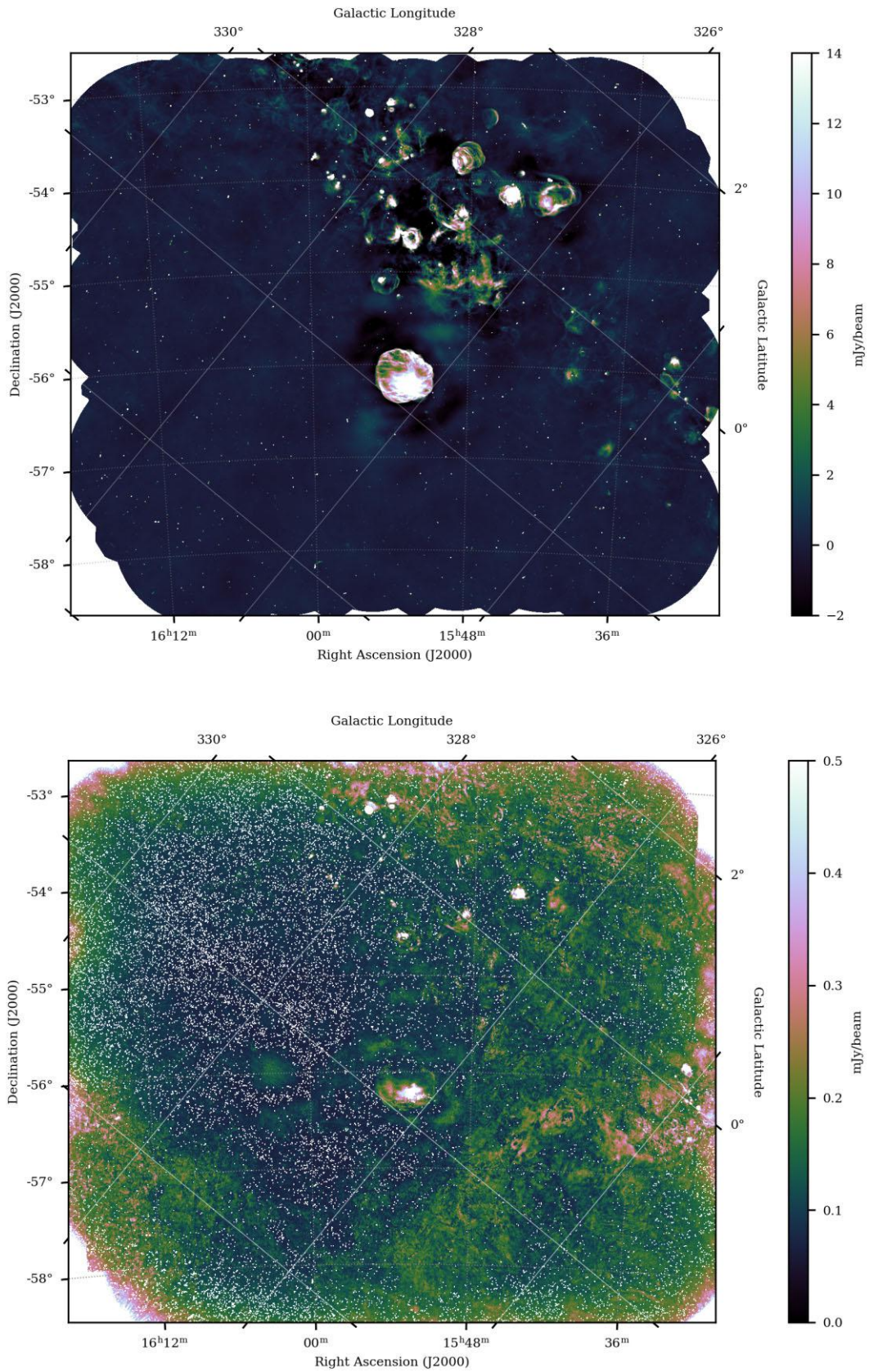


**Figure 1.** The top image shows the EMU/POSSUM Galactic pilot II field as observed by ASKAP at 933 MHz in total intensity with an angular resolution of 18". The bottom image shows the same field in PI.

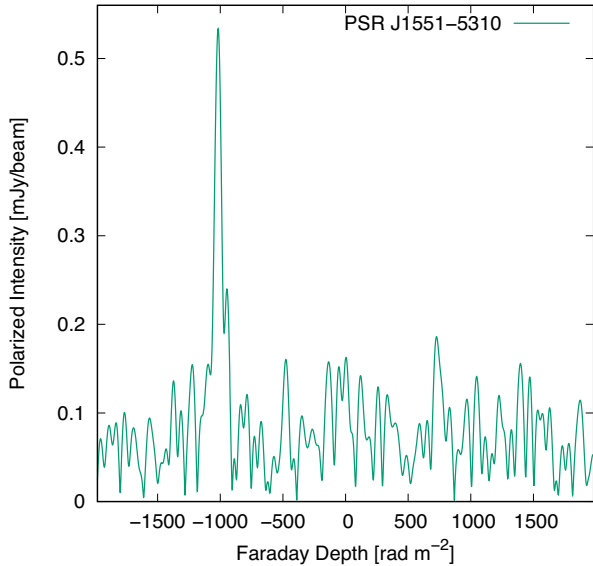


**Figure 2.** FD spectrum of the pulsar J1551–5310, which is located inside SNR candidate G328.0 + 0.7.

For the known SNRs and our candidates, we did not use the FD cube from the POSSUM pipeline, but calculated them ourselves. We used the Q and U data cubes from scheduling block 43 773. Instead of a Fourier transform, we de-rotated the Q and U data in each frequency channel for each rotation measure (RM). We probed an RM range from  $-2000$  to  $+2000$   $\text{rad m}^{-2}$  with a step size of  $1$   $\text{rad m}^{-2}$ . A sample FD function is shown in Fig. 2. This was taken towards the pulsar PSR J1551–5310 inside our SNR candidate G328.0 + 0.7. The RM for this pulsar is catalogued by Han et al. (2018) to be  $-1023.3 \pm 6.3$   $\text{rad m}^{-2}$ . In our data, we find  $RM = -1017 \pm 5$   $\text{rad m}^{-2}$ .

## 2.2 Ancillary data

In addition to the radio data from ASKAP, we utilize images of the same field of the Galactic plane from two other sky surveys. Comparing radio and MIR fluxes is a commonly used technique for identifying SNRs. Thus, we make use of  $12$   $\mu\text{m}$  infrared data from WISE (Widefield Infrared Survey Explorer) (Wright et al. 2010) with an angular resolution of  $6.5''$  as part of the candidate identification process, further outlined in Section 3.2.1. We use  $12$   $\mu\text{m}$  data because it traces emission from hot dust and PAHs, both of which are expected to be abundant in H II regions (Anderson et al. 2014) and largely destroyed in SNRs (Slavin, Dwek & Jones 2015). Pixel values in WISE data are measured in digital number (DN) units, which are designed for relative photometric measurements (Cutri et al. 2013) and are sufficient for our purposes.

We use low frequency (198 MHz) data from GLEAM (The Galactic and Extragalactic All-sky MWA survey) (Wayth et al. 2015) to calculate spectral indices for some remnants, the details of which are provided in Section 3.2.2. The angular resolution of the GLEAM data ( $\sim 169'' \times 149''$ ) is relatively poor compared to the resolution of ASKAP so while we are able to calculate spectral indices for six of the known remnants, we can obtain indices with these data for only two of our candidates.

## 2.3 Flux integration

To calculate total intensity flux densities, we use a combined map that was created by averaging data from the two ASKAP second pilot observations. This was done to minimize the effect of background fluctuations.

Because of the complexity of the background, different methods for calculating flux densities and performing background subtraction were explored. Integrating over radial profiles using Karma software (Gooch 1995) did not allow us to properly account for variations in the background or surrounding bright sources. Attempting to use a circular aperture to define the source with multiple circular apertures defining the background, as done by Anderson et al. (2017), presented similar challenges and lacked consistency. Ultimately, flux integration was performed using the POLYGON\_FLUX software, which was developed by Hurley-Walker et al. (2019) for the GLEAM survey to deal with extended sources that have complicated backgrounds. The software calculates the flux density within a chosen region, subtracts user-selected point sources, and performs background subtraction, allowing the user to select surrounding regions that should not be included as part of the background.

For each source, the calculations were performed multiple times in order to obtain a more accurate flux value and an error estimate. Three different definitions of the background were used to estimate the systematic uncertainty due to flux aperture definition. The calculations were run using backgrounds defined as 4–10, 10–16, and 16–22 pixels from the source (with a pixel size of  $2''$ ). Additionally, the source and background selection process was performed at least twice for each source to account for uncertainties resulting from the definition of the source perimeter. Thus, the flux density calculations were run at least six times per source. The flux densities in Table 1 were taken as the median values of these calculations and the errors were determined by the range between the extrema. Instrumental uncertainties in the fluxes were found to be relatively insignificant compared to the systematic estimates and were not included.

## 3 RESULTS

### 3.1 The EMU/POSSUM Galactic pilot field

Fig. 3 shows the EMU/POSSUM Galactic pilot II data as observed by ASKAP and the same field in the MIR as observed by WISE (Wright et al. 2010). The field looks across the Galactic plane, with an approximate longitude and latitude of  $323^\circ \leq l \leq 330^\circ$  and  $-4^\circ \leq b \leq 2^\circ$ , respectively, along a tangent to the Norma arm and across several other spiral arms. This gives us a long line of sight through the inner Galaxy, up to distances of about 18 kpc.

The annotations shown in Fig. 3 indicate the locations of the known SNRs (green) and H II regions (blue) within this field as well as the locations of our 21 SNR candidates (white). The known SNRs are taken from the Green (2022) radio SNR catalogue and the H II regions come from the WISE Catalogue of Galactic H II regions (Anderson et al. 2014). There are eight known SNRs in this field, including one that we believe should be reclassified as multiple sources (discussed further in Section 4). One of the known SNRs lies at the edge of the field and is only partially imaged in the combined map as shown.

This field was selected in part because it can be broken into two regions that are visually and meaningfully distinct in both the radio and MIR. The upper left part of the field looks along a tangent to the Norma arm and thus we see a high density of H II regions and thermal emission. The lower right part of the field is noticeably fainter with less background emission and a lower density of H II regions. This

**Table 1.** Known SNRs and SNR candidates in the EMU/POSSUM Galactic pilot II field. Surface brightnesses are given at 933 MHz. Spectral indices are calculated using the 933 MHz flux value from ASKAP and the 198 MHz flux value from GLEAM.

Name	RA (J2000)	Dec (J2000)	Size [']	Flux density [Jy at 933 MHz]	Surface brightness [ $10^{-21} \text{Wm}^{-2} \text{Hz}^{-1} \text{sr}^{-1}$ ]	Polarization Detected	Spectral index (with GLEAM)
Known SNRs							
G326.3 – 1.8	15:52:59	–56:07:27	38	$148 \pm 3$	$15.4 \pm 0.3$	Y	$-0.27 \pm 0.02$
G327.1 – 1.1	15:54:26	–55:05:59	18	$7.3 \pm 0.2$	$3.4 \pm 0.1$	Y	$-0.1 \pm 0.1$
G327.2 – 0.1	15:50:57	–54:18:00	5	$0.50 \pm 0.05$	$3.0 \pm 0.3$	Y?	$-0.4 \pm 0.1$
G327.4 + 0.4	15:48:23	–53:46:13	21	$26.1 \pm 0.4$	$8.9 \pm 0.1$	Y	$-0.44 \pm 0.01$
G327.4 + 1.0	15:46:53	–53:19:51	14	$1.92 \pm 0.07$	$1.47 \pm 0.05$	Y?	$-0.3 \pm 0.1$
G328.4 + 0.2	15:55:32	–53:17:02	5	$15.3 \pm 0.3$	$92 \pm 2$	N/A**	$-0.1 \pm 0.1$
SNR Candidates							
G323.2 – 1.0	15:31:40	–57:23:42	7	$0.32 \pm 0.01$	$0.97 \pm 0.04$	N	
G323.6 – 1.1*	15:34:03	–57:21:42	$34 \times 20$	N/A	N/A	N	
G323.6 – 0.8*	15:32:56	–57:02:53	$28 \times 23$	<1	<0.3	N	
G323.7 + 0.0	15:30:39	–56:19:26	3	$0.07 \pm 0.02$	$1.1 \pm 0.3$	N	
G323.9 – 1.1*	15:36:24	–57:08:45	$29 \times 18$	<1	<0.3	N	
G324.1 – 0.2	15:33:34	–56:13:59	$10 \times 9$	$0.26 \pm 0.03$	$0.43 \pm 0.06$	N	
G324.1 + 0.0	15:32:37	–56:03:05	$11 \times 7$	$1.0 \pm 0.1$	$1.9 \pm 0.2$	N	$-0.3 \pm 0.2$
G324.3 + 0.2	15:32:45	–55:47:45	4	$0.120 \pm 0.008$	$1.13 \pm 0.08$	N	
G324.4 – 0.4	15:36:00	–56:14:08	$18 \times 13$	$0.44 \pm 0.09$	$0.28 \pm 0.06$	N	
G324.4 – 0.2	15:35:26	–56:04:08	$3 \times 2$	$0.006 \pm 0.001$	$0.14 \pm 0.02$	N	
G324.7 + 0.0	15:36:06	–55:46:29	4	$0.055 \pm 0.005$	$0.52 \pm 0.04$	N	
G324.8 – 0.1	15:37:07	–55:45:03	$25 \times 20$	<1	<0.3	N	
G325.0 – 0.5	15:39:43	–55:58:29	$34 \times 28$	<6	<0.9	N	
G325.0 – 0.3	15:39:14	–55:49:52	4	$0.19 \pm 0.01$	$1.7 \pm 0.1$	N	
G325.0 + 0.2	15:37:02	–55:26:56	5	$0.11 \pm 0.01$	$0.66 \pm 0.08$	N	
G325.8 – 2.1	15:52:03	–56:46:04	$36 \times 30$	N/A	N/A	N	
G325.8 + 0.3	15:41:15	–54:54:26	28	N/A	N/A	N	
G327.1 + 0.9	15:45:59	–53:32:33	2	$0.019 \pm 0.004$	$0.7 \pm 0.1$	N	
G328.0 + 0.7	15:51:41	–53:10:11	8	$0.50 \pm 0.06$	$1.2 \pm 0.1$	Y?	
G328.6 + 0.0	15:57:31	–53:22:05	$34 \times 19$	$3.5 \pm 0.9$	$0.8 \pm 0.2$	N	$-0.75 \pm 0.06$
G330.2 – 1.6	16:12:32	–53:27:01	9	$0.08 \pm 0.02$	$0.14 \pm 0.04$	N	

Note. \*Currently classified as a single source (G323.7 – 1.0). \*\*Leakage.

allows us to test our ability to detect SNR candidates in each of these regions. Since we are primarily expecting to find low surface brightness sources, it is probable that there are candidates in the upper left region of the Galactic plane that we are unable to detect due to the high concentration of thermal emission. The locations of the candidates in Fig. 3 support this as they are clearly concentrated in areas with fewer H II regions and less background emission.

### 3.2 SNR identification and verification

A SNR is formed in the aftermath of a stellar explosion as the ejected material expands into the ISM bounded by a supersonic shock wave that sweeps up interstellar material and magnetic fields as it travels. At the shock front, electrons are accelerated to relativistic speeds and interact with the magnetic field to produce highly linearly polarized synchrotron emission that is best observed in the radio (van der Laan 1962). A SNR can typically be identified by the distinctive shell-like structure that is formed through this interaction between the supernova shock and the ISM. The structural evolution of the remnant will depend on factors like the characteristics of the explosion, the density of the surrounding ISM, and the ambient magnetic field (Whiteoak & Gardner 1968; Truelove & McKee 1999; Kothes & Brown 2009). While these factors may result in asymmetries, we generally expect to see well-defined rounded edges, produced by the shock, with fainter emission coming from the remnant’s centre.

Here, we identify SNR candidates primarily by looking for radio-emitting shell-like structures that lack clear MIR counterparts. After identifying candidates, we attempt to find further evidence that they

are SNRs. First, the presence of a young pulsar indicates that a supernova explosion has recently occurred so spatial coincidence of a candidate with this type of star can significantly increase our confidence in its classification. Second, radio emission from SNRs is primarily non-thermal synchrotron emission that can be differentiated from thermal emission using polarization and spectral indices. Non-thermal synchrotron emission is associated with a steep negative spectral index and linear polarization while thermal optically thin free–free emission is associated with a flat, unpolarized spectrum. As we are observing at relatively low radio frequencies, we can also expect to find compact H II regions with optically thick free–free emission and steep positive spectral indices.

#### 3.2.1 Radio and MIR emission

Comparing radio and MIR fluxes is a commonly used technique for distinguishing non-thermal SNR emission from thermally emitting sources like H II regions (Whiteoak & Green 1996; Helfand et al. 2006; Green et al. 2014; Anderson et al. 2017). H II regions produce MIR emission primarily through stochastic heating of small dust grains and the vibrational and bending modes of PAHs (Draine 2011). Supernovae are known to produce significant amounts of dust and SNRs can also produce MIR emission through these thermal processes. However, this emission is relatively weak. This is in part because most dust (>90 per cent) in SNRs is found in the dense, cool gas phase, rather than the X-ray emitting plasmas, resulting in a spectral energy distribution that peaks at longer infrared wavelengths



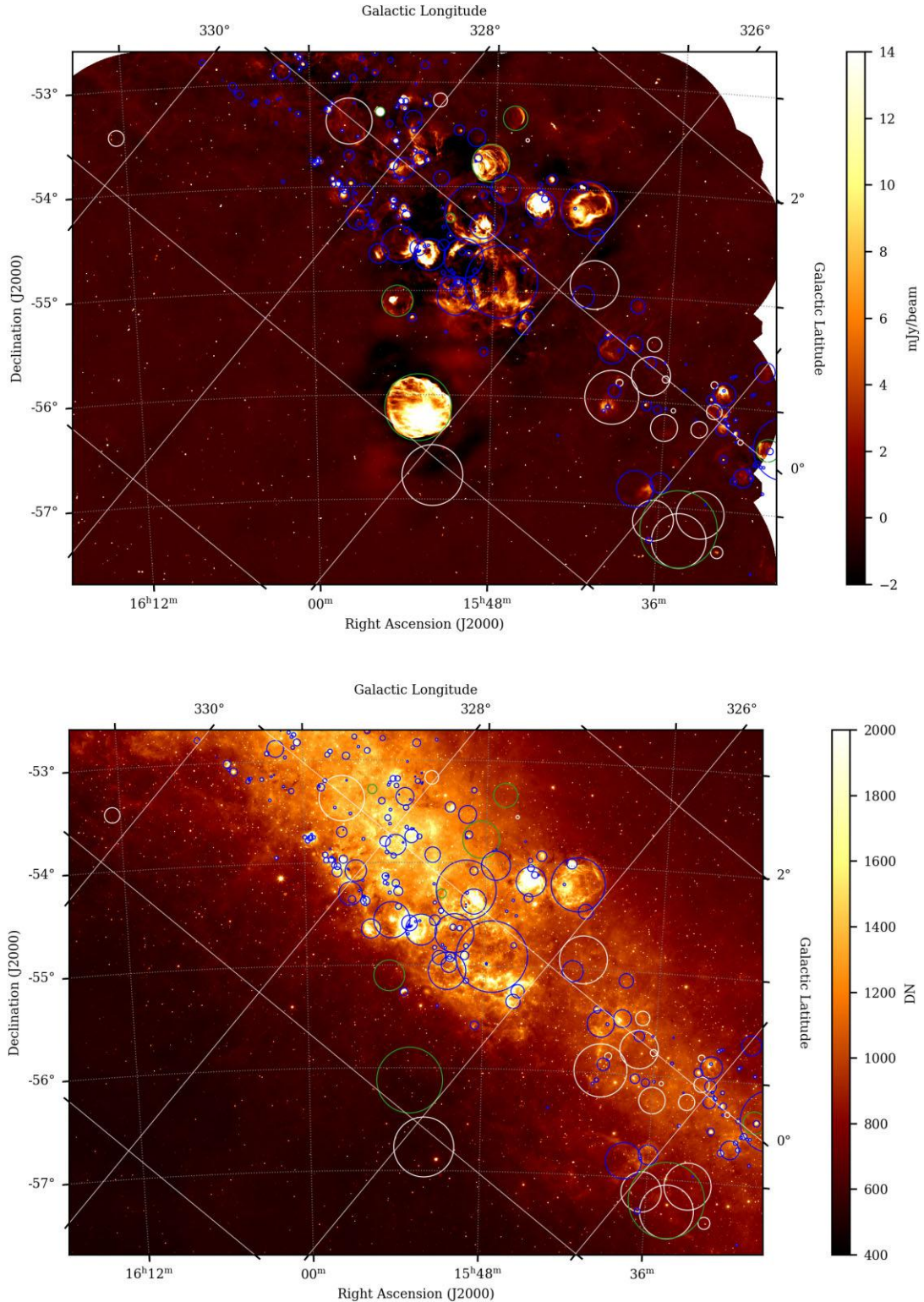


**Figure 3.** The top image shows the EMU/POSSUM Galactic pilot II field from ASKAP at 933 MHz in total intensity. The bottom image shows the same field in the MIR from WISE ( $12\ \mu\text{m}$ ). The green circles show the locations of known SNRs, taken from Green (2022). The blue circles indicate the locations of known H II regions, taken from Anderson et al. (2014). The white circles indicate the locations of our SNR candidates.

than studied here (Priestley et al. 2022). Additionally, while the supernova shock can heat dust grains, it can also result in the destruction of a significant amount of dust and large molecules like PAHs (Slavin et al. 2015). According to Bianchi & Schneider

(2007), only 2 per cent–20 per cent of the initial dust mass survives the passage of the reverse shock, depending on the density of the surrounding ISM. Therefore, dust emission from SNRs is typically expected to be weak, if it is detectable at all, and importantly it has

been shown that SNRs have significantly lower MIR to radio flux ratios when compared to H II regions (Whiteoak & Green 1996; Pinheiro Gonçalves et al. 2011). Thus, while some SNRs do emit in the MIR, sources that lack MIR emission are unlikely to be H II regions.

We began our search for SNR candidates by comparing the radio data from ASKAP to MIR data from WISE. The images used can be found in Fig. 3. Because of the small size of the field, we were able to perform a detailed search by eye, specifically looking for shell-like structures in the radio that do not have MIR counterparts. This was done separately by two of the authors before comparing results. To simplify the search, we eliminated sources that had already been classified as H II regions. The WISE Catalogue of Galactic H II Regions (Anderson et al. 2014) was used to identify all known H II regions in the field. The catalogue was made using 12  $\mu\text{m}$  and 22  $\mu\text{m}$  data from WISE and includes over 8000 Galactic H II regions and H II region candidates. We use Version 2.2 of the catalogue, downloaded from <http://astro.phys.wvu.edu/wise/>, and include all listed entries. We did not find any sources in our field that we believe to be H II regions that were not already part of the WISE H II region catalogue. Specifically, we did not find any new extended sources that were clearly visible in both radio and MIR. Thus, the radio to MIR comparison was not used to rule out any potential candidates but instead served primarily as evidence that our candidates are not H II regions.

### 3.2.2 Spectral indices

Spectral indices can help to differentiate thermal and non-thermal emission. We assume the relation  $S(\nu) \propto \nu^\alpha$ , where  $S$  represents the flux density,  $\nu$  represents the frequency, and  $\alpha$  represents the spectral index. The synchrotron spectral index is determined by the power-law energy distribution of relativistic particles, which are accelerated through multiple crossings at the shock front in a process known as diffusive shock acceleration (DSA) (Bell 1978; Blandford & Ostriker 1978). For a shell-type remnant, linear DSA predicts a spectral index of  $-0.5$  and observations show that most catalogued Galactic SNRs have a spectral index within the range  $\alpha = -0.5 \pm 0.2$  (Reynolds, Gaensler & Bocchino 2012; Dubner & Giacani 2015). However, there is significant uncertainty in many of the measured values and outliers do exist.

Thermally emitting H II regions are expected to have flatter spectral indices for optically thin free-free emission, generally around  $-0.1$ , or steep inverse spectra, around  $+2$ , for optically thick. Pulsar wind nebulae (PWNe), or centre-filled SNRs, tend to have flatter spectra as well, usually within the range  $-0.3 \leq \alpha \leq 0.0$ , though in rare cases they can be as steep as  $-0.7$  (Kotthes 2017). PWNe accelerate relativistic particles through a different mechanism, the interaction of the pulsar wind with the supernova ejecta, which typically results in a flatter particle energy distribution. Thus, PWNe can be more difficult to distinguish from thermal sources when they do not have a visible shell component. This is not the only inherent bias against detecting these types of sources as they are also generally smaller and have a less visually distinct morphology. In fact, only 3 per cent of catalogued Galactic SNRs are shell-less PWNe (Dubner 2017).

We calculate spectral indices using data from GLEAM (Wayth et al. 2015) for sources that are large enough and bright enough to be detected in the highest frequency band of the GLEAM survey. These appear to be sources that are at least  $5'$  in diameter with a flux density of around 1 Jy in the GLEAM band. This includes all of the known SNRs in the field but only two of our SNR candidates. The

GLEAM flux densities were calculated using the method outlined in Section 2.3. These spectral indices can be found in Table 1 with errors based on the uncertainties of the flux densities. Attempts were made to calculate in-band spectral indices with the ASKAP pilot II data but the uncertainties were too significant to produce meaningful results. Follow up observations at a second frequency would be valuable in allowing for the calculation of spectral indices for sources that are not visible in the GLEAM survey.

### 3.2.3 Polarization

Detection of linearly polarized radio emission is strong evidence that an extended Galactic radio nebula is a SNR. SNRs emit highly linearly polarized synchrotron emission. The degree of polarization can be intrinsically more than 70 per cent. For the SNR G181.1 + 9.5, in both the Effelsberg 5 GHz observations and 1.4 GHz observations with the synthesis telescope at the Dominion Radio Astrophysical Observatory (DRAO ST), Kotthes et al. (2017) find polarization of about 70 per cent. G181.1 + 9.5 is a highly evolved SNR with a highly compressed and very regular magnetic field in its shell. Conversely, young SNRs typically have much lower intrinsic degrees of polarization as they display significant turbulence in their expanding shells. The lowest polarization observed at a high radio frequency in an SNR is possibly the 2 per cent observed in SNR G11.2 – 1.1 at a frequency of 32 GHz (Kotthes & Reich 2001).

EMU and POSSUM observe at radio frequencies between 800 and 1087 MHz. At these low frequencies, Faraday rotation strongly affects polarized signals. There is foreground Faraday rotation in the magneto-ionic medium between us and the nebula and there may be internal effects inside the SNR's shell. In the SNR's shell we find a mix of synchrotron emitting and Faraday rotating plasmas, which means that internally the synchrotron emission may be affected by different amounts of Faraday rotation depending on where the emission comes from within the shell. Integrating this emission along the line of sight through the emission region may lead to significant depolarization. These effects become significantly worse at low frequencies as the amount of depolarization is inversely proportional to the frequency squared. Faraday rotation in the foreground ISM may also lead to depolarization, especially if the foreground path traverses turbulent ionized areas such as H II regions, or even spiral arms.

Because we are observing at a relatively low frequency, failure to detect polarization should not be considered evidence that a candidate is not an SNR, especially considering that many of our candidates are small or faint sources that may be located at far distances across the Galactic plane. The probability of detecting polarization from our SNR candidates is higher for high latitude sources, as their foreground likely does not contain any turbulent ionized regions. SNRs located close to the plane of the Galaxy may suffer from foreground depolarization caused by overlapping H II regions in the foreground or parts of a spiral arm between the SNR and us as spiral arms contain enhanced electron densities and magnetic fields.

Distinguishing between real and instrumental polarization is an additional challenge. As shown by the PI data in Fig. 1(b), we see evidence of instrumental effects at the positions of known H II regions. Particularly for bright sources, we believe that polarization with a smooth structure that closely resembles what is seen in total power is potentially the result of Stokes I leakage. Polarization that has a speckled appearance is more likely to be real as this indicates a changing RM, or intrinsic polarization angle, on small scales. For



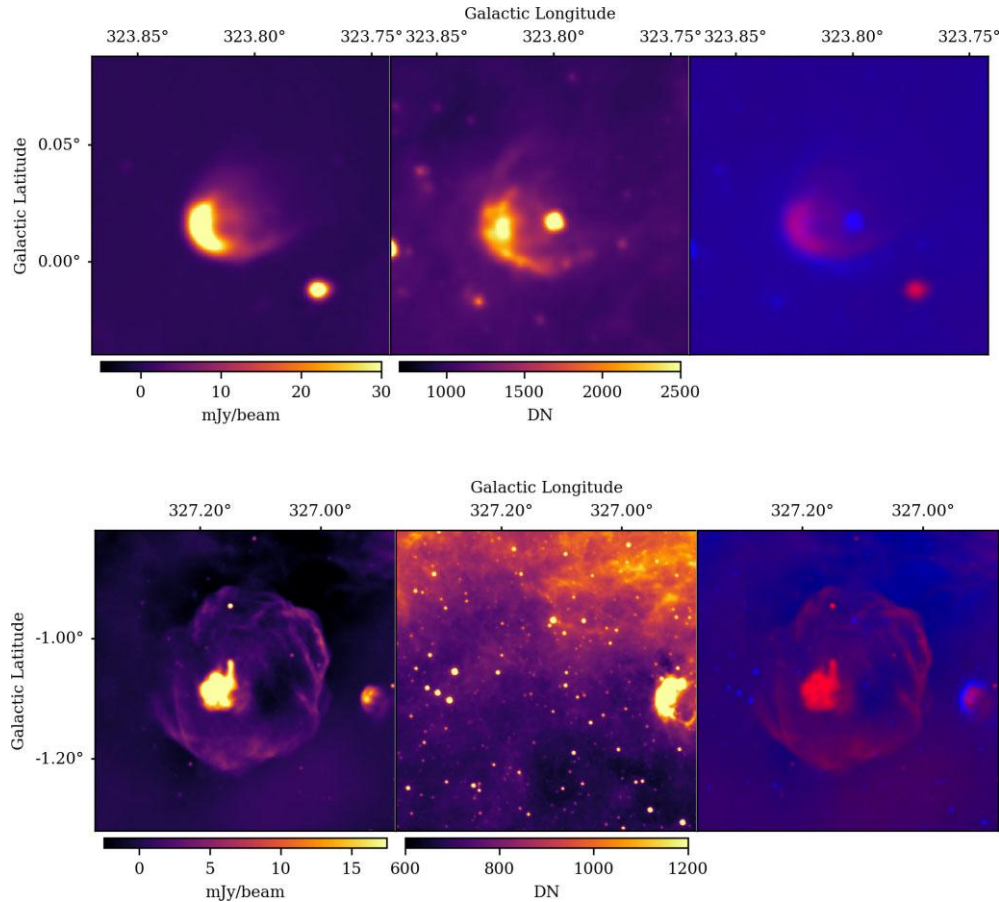


**Figure 4.** Comparing radio and MIR emission from an H II region and an SNR. From left to right, the top images show an H II region in radio (from ASKAP), MIR (from WISE), and a combined image with radio in red and MIR in blue. The bottom images show the same data for a known SNR, G327.1 – 1.1, and demonstrate the absence of an MIR counterpart.

further evidence of real polarization, we look for structures that are contained entirely within the SNR and that appear similar in the PI and RM maps. Real polarization from the SNR should be distinct from what is seen in the surrounding background in intensity and RM.

We detect polarized signal significantly above the noise from all known SNRs in our field, but we are not convinced that all of it is real. Further details for each source are provided in Section 3.3. Similarly to Dokara et al. (2018), we are mostly unsuccessful in detecting polarization from Galactic SNR candidates. We are only able to detect what we believe to be real polarization from one of our candidates, G328.0 + 0.7. The details of this can be found in the candidate description in Section 4.1.

### 3.3 Characteristics of known SNRs

As discussed in Section 3.2.1, SNRs can be identified by looking for extended radio sources that lack a MIR counterpart. The top images in Fig. 4 show a known H II region that could potentially be misidentified as an SNR based solely on its radio morphology. The presence of a clear counterpart in the MIR helps to correctly identify this source as an H II region. The bottom images in Fig. 4 show a known SNR, G327.1 – 1.1, and its clear lack of MIR emission. A small H II region can be seen along the right edge of the SNR images in both the radio and the MIR, further illustrating this distinction.

There are eight known SNRs in the EMU/POSSUM Galactic pilot II field that appear in the Green (2022) catalogue. We believe G323.7 – 1.0 should be reclassified as three separate sources so it is discussed under the candidates section. Our observations of the other seven known SNRs are discussed here. The 933 MHz ASKAP images of the SNRs can be found in Fig. 5. More detailed images of the known SNRs in both radio and MIR, which include coordinate axes and colour bars, can be found in Appendix A.

#### 3.3.1 G323.5 + 0.1

This source is a shell-type SNR that lies at the edge of our field. It is only fully imaged in the ASKAP data at low frequencies so it has not been studied here in-depth and thus does not appear in Table 1. Fig. A1 was made using a 48-MHz wide channel centred at 823.5 MHz since the source is not fully visible in the higher frequency channels. The source overlaps with a bright H II region that can be seen in MIR.

#### 3.3.2 G326.3 – 1.8, MSH 15 – 56

This SNR is a composite source, a bright pulsar wind nebula with a well-defined radio shell. It is the largest SNR in the field with a size of 38'. Bright filamentary emission can be seen coming from the shell. The PWN is offset to the west of the remnant's centre and is elongated in the north–south direction (Fig. A2). The source is

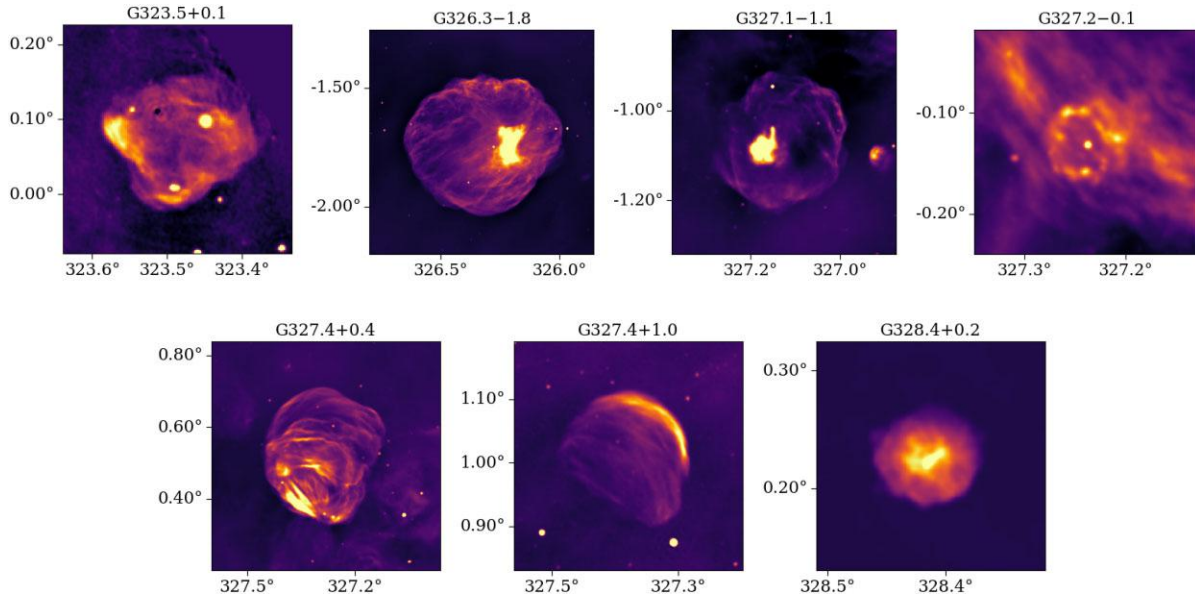


**Figure 5.** 933 MHz images of the seven known SNRs with Galactic longitude on the  $x$ -axis and Galactic latitude on the  $y$ -axis. For more detailed images with colour bars, see Appendix A.

estimated to be at a distance of 3.5–5.8 kpc (Ranasinghe & Leahy 2022). There is clear polarization, mostly concentrated around and extending from the PWN (Fig. 6). This can be seen in both the PI and RM maps. There is also some polarization coming from the east side of the shell. We believe all of this polarization is real since it is not smooth and aligns with what is expected from total power without mirroring it exactly, which could indicate leakage. It also has a high negative RM and there is almost no polarized emission coming from the background in this part of the field it could be confused with.

### 3.3.3 G327.1 – 1.1

This SNR is another composite source with a bright pulsar wind nebula and a relatively faint shell that is likely missing some short spacings in the ASKAP data. This is evidenced by the negative bowls of emission, seen in Fig. 4(b). There is a bright H II region located to the west of the SNR. The remnant is believed to be located at a distance of 4.5–9 kpc (Sun, Wang & Chen 1999; Wang et al. 2020), indicating it is likely located within or near the Norma arm. There is obvious polarization coming from the PWN but no clear polarization coming from the shell (Fig. 6). We believe this polarization to be real because it is contained entirely within the PWN and is not smooth.

### 3.3.4 G327.2 – 0.1

This source is believed to be a shell-type remnant associated with a young magnetar, J1550-5418, located near its centre (Gelfand & Gaensler 2007). The magnetar has a characteristic age of 1.4 kys and a RM of  $-1860 \pm 20 \text{ rad m}^{-2}$  (Camilo et al. 2007, 2008). Distance estimates for the shell are between 4 and 5 kpc (Tiengo et al. 2010) while the magnetar has been estimated to be at a distance of 9 kpc (Camilo et al. 2007). The source lies on a larger filament of emission that is likely unrelated to the SNR (Fig. A3). While we were not able to detect any clear real polarization coming from the shell due to confusion with the background, there does seem to be real polarization coming from the centre (Fig. 6). Specifically, there are two peaks in the RM for the central point source. We believe the

first peak, around  $-1820 \text{ rad m}^{-2}$ , comes from the pulsar and we speculate that the second peak, around  $15\text{--}30 \text{ rad m}^{-2}$ , may come from a previously undetected pulsar wind nebula.

### 3.3.5 G327.4 + 0.4, Kes 27

This shell-type SNR exhibits multiple shell structures and many internal filaments. There is a small overlapping H II region that can be seen in both radio and MIR (Fig. A4). H I absorption suggests the SNR is located at a distance of 4.3–5.4 kpc (McClure-Griffiths et al. 2001) while optical extinction suggests a distance of 2.8 kpc (Wang et al. 2020). We detect polarization coming from several parts of the remnant (Fig. 6). We believe the polarization seen along the north-east edge of the remnant to be real as it is distinct from the total power structure, and thus cannot be leakage, and has a high positive RM that is distinct from the RM found in the rest of the image. The polarization in the south-east may be real as well but this is not certain as the smoother appearance and flatter RM may indicate that it is instrumental. There is also some polarization near the centre of the remnant that has a high negative RM and may be real but this is also unclear.

### 3.3.6 G327.4 + 1.0

This source is an asymmetrical shell that is brightest along the north-western edge. There is also some faint central emission with filaments that curve in the same direction as the shell (Fig. A5). There is potential polarization coming from the centre of the remnant but it is not strong enough to be definitively distinct from the background features seen in the south (Fig. 6e). However, the positive RM seems to be mostly confined to the source with some extending to the north of the remnant. This extension is somewhat mirrored in total power, possibly indicating that some of this polarization is real but this is not conclusive.



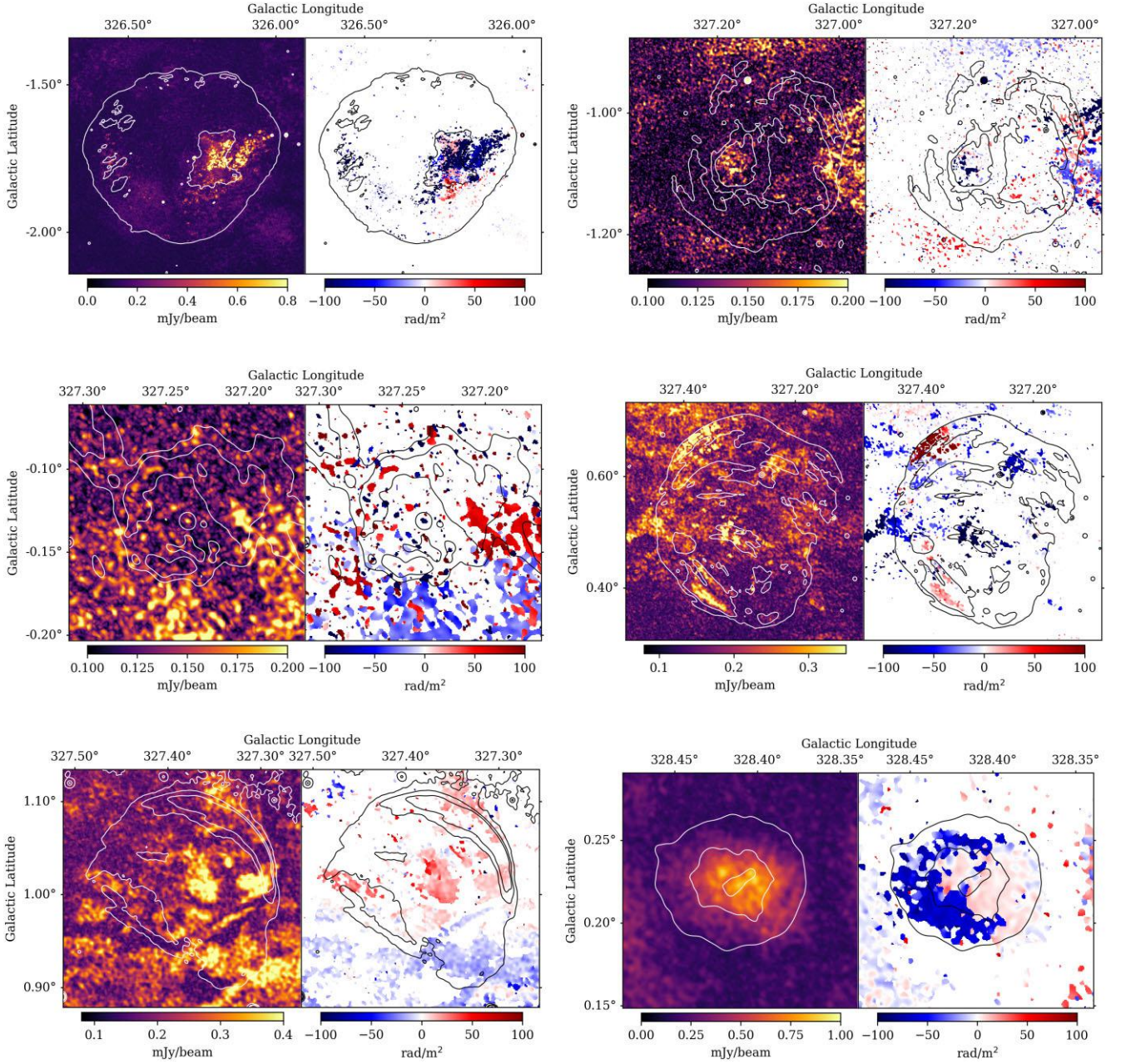


**Figure 6.** For each source, the left-hand image shows PI and the right-hand image shows Faraday RM. The contours are used to indicate the total power structures. From left to right, top row: G326.3 – 1.8, G327.1 – 1.1. Middle row: G327.2 – 0.1, G327.4 + 0.4. Bottom row: G327.4 + 1.0, G328.4 + 0.2.

### 3.3.7 G328.4 + 0.2, MSH 15 – 57

This SNR is believed to be the largest and most radio luminous pulsar wind nebula in our galaxy (Gaensler, Dickel & Green 2000). It has no visible shell but there is a central bar structure that runs in the south-east to north-west direction (Fig. A6). It is believed to be located at a distance of over 16.7 kpc (Ranasinghe & Leahy 2022) placing it along the outer edge of the Galaxy. The source appears to be polarized but because it is so bright we believe this is likely the result of leakage. In RM we see two components, a high negative component and a low positive component. The high negative component extends over the remnant and has a similar structure to what is seen in PI. The low positive component seems to be concentrated to the west side of the PWN (Fig. 6).

### 3.4 Spectral indices of known remnants

For each of the known SNRs, we calculate a spectral index using the 933 MHz flux density from ASKAP and the 198 MHz flux density value from GLEAM. These indices can be found in Table 1. Fig. 7 shows the ASKAP and GLEAM flux densities calculated in this paper plotted with flux densities taken from Green (2019) and references therein. The spectral indices seen on the plots are calculated using the slopes of the fit lines, which are made using the literature values as well as the ASKAP and GLEAM values. We use this second method of calculating spectral indices to evaluate whether or not the indices found using only the ASKAP and GLEAM data are reliable.

G326.3 – 1.8 is a composite source that has been shown to have an intermediate index ( $\sim -0.3$ ) with a flatter component coming



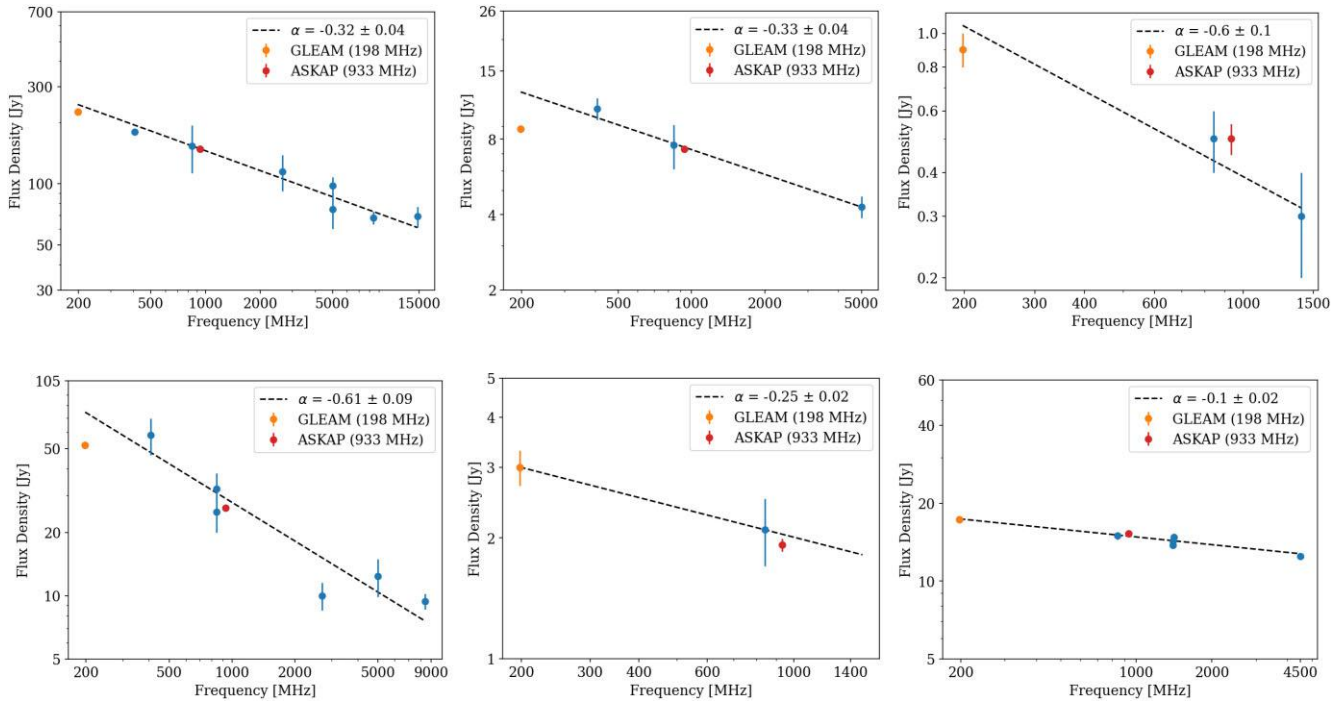


**Figure 7.** Flux densities of known SNRs. From left to right, top row: G326.3 – 1.8, G327.1 – 1.1, and G327.2 – 0.1. Bottom row: G327.4 + 0.4, G327.4 + 1.0, and G328.4 + 0.2. The red and orange data points are the values calculated in this paper using ASKAP and GLEAM data, respectively. The blue data points represent the flux densities of known SNRs taken from Green (2019) and references therein. 20 per cent errors are assumed if none were given.  $\alpha$  represents the spectral index as determined by the slope of the linear fit.

from the PWN and a steeper component coming from the shell (Dickel, Milne & Strom 2000). The values we obtain are in moderate agreement with each other and are consistent with the expected value for this source.

G327.1 – 1.1 is also a composite source that is believed to have an intermediate index ( $-0.36$ ; Clark, Caswell & Green 1975). The flux value we obtain from the GLEAM data appears to be too low, as demonstrated by the plot, resulting in a spectral index that is likely too flat. The value obtained from the fit is consistent with what is expected and is likely more reliable.

G327.2 – 0.1 is believed to be a shell-type remnant though it is associated with a known magnetar and could be a composite source. The values we obtain are in moderate agreement though they have relatively large errors. Both are consistent with what is expected for non-thermal emission from a shell-type remnant.

G327.4 + 0.4 is also a shell-type remnant. The values we obtain are not in agreement though both are consistent with the expected index of a shell-type remnant. The plot appears to indicate that the GLEAM flux value may be too low.

G327.4 + 1.0 is a shell-type remnant for which there was previously only one flux measurement (Whiteoak & Green 1996) so the spectral index derived from the linear fit may be less reliable. The values we obtain are consistent with each other and although they are flat for a shell-type remnant, they are not unreasonable for this type of source. Given that many of the GLEAM fluxes seem to be lower than expected, and because our fit is based on only three data points, the spectral index of this source may be steeper than the values we have calculated here.

G328.4 + 0.2 is a shell-less PWN that has been shown to have a flat spectral index (Gaensler et al. 2000; Gelfand et al. 2007). The values we obtain are consistent with each other and with what is expected for a typical pulsar wind nebula.

While the spectral indices we calculate using these two methods are generally in agreement with each other and with the expected values for the corresponding SNR types, many of these values have relatively large errors. The values obtained from the linear fit should be considered to be more reliable than the values provided in Table 1 as the deviations seem to mostly be the result of lower than expected values for the GLEAM fluxes, particularly for the fainter remnants. Thus, the spectral indices we calculate for our candidates using this data should be viewed with a level of skepticism. High resolution data at a second frequency will likely be required to produce reliable spectral indices for the SNR candidates.

#### 4 SNR CANDIDATES

The locations of our SNR candidates are indicated in Fig. 3. Notably, the candidates are highly concentrated in the lower right corner of the image. We believe we were able to detect more candidates in this part of the field because of the relatively low density of H II regions compared to the upper left half of the image. This may seem to contradict what is expected as the true SNR density is likely to be higher within spiral arms, not away from them. Thus, we believe it is highly probable that there are faint sources within the Norma arm region of the field that we were unable to detect due to the high concentration of thermal emission and H II regions.

Data collected for known and candidate SNRs is shown in Table 1. Right ascension and declination are determined by fitting an ellipse to the source using CARTA software (Comrie et al. 2021) and taking the central coordinates of the ellipse. The sizes of the sources are determined by taking the major and minor axes of these ellipses.

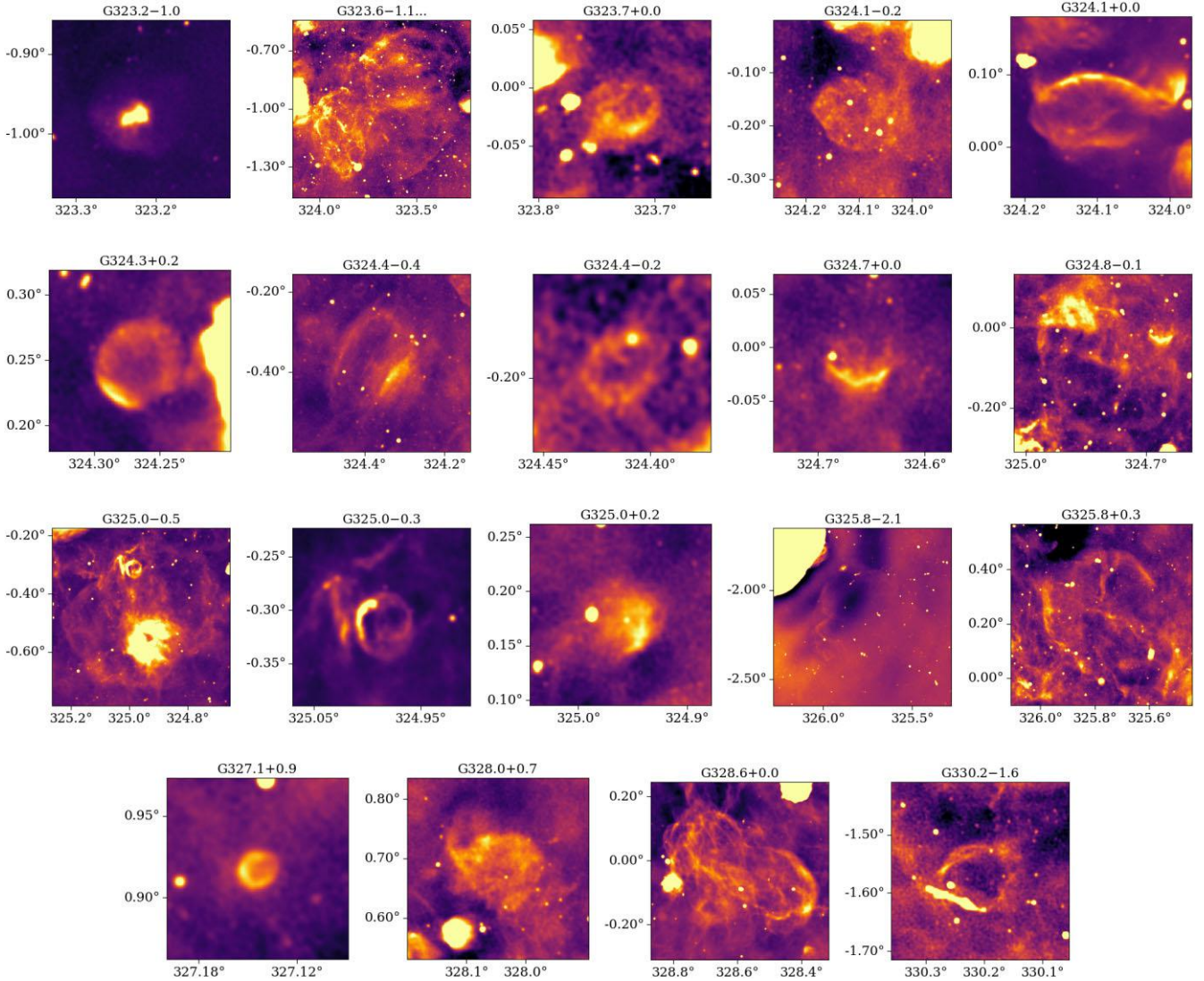


**Figure 8.** 933 MHz images of the SNR candidates with Galactic longitude on the  $x$ -axis and Galactic latitude on the  $y$ -axis. For more detailed images with colour bars, see Appendix B.

#### 4.1 Characteristics of SNR candidates

Here, we list 21 SNR candidates, three times the number of known SNRs in this field. We believe some of these sources to be strong SNR candidates while others are weaker and will require further observations to determine if they are indeed SNRs. We define the strength of our candidates based on whether or not we are able to find evidence of other expected SNR properties, such as polarization or a steep negative spectral index. Only two of the candidates were visible in the GLEAM data, allowing us to calculate spectral indices, and only one shows clear evidence of real polarization. The 933 MHz images of the candidates can be found in Fig. 8. More detailed images of the SNR candidates in both radio and MIR, which include coordinate axes and colour bars, can be found in Appendix B.

##### 4.1.1 G323.2 – 1.0

This source has the morphology of a pulsar wind nebula with a very faint shell. As shown in Fig. B1, there is an infrared source that overlaps with the PWN but the IR source has a different morphology

and has been identified as a star by Cutri et al. (2003). The shell is roughly circular and the PWN has a similar shape to the PWN of G326.3 – 1.8, but elongated along the east–west axis. This source was listed as an SNR candidate by Whiteoak & Green (1996) but was not confirmed and no image was provided.

##### 4.1.2 G323.6 – 1.1, G323.6 – 0.8, and G323.9 – 1.1

This object is currently classified as a single source in Green’s catalogue, G323.7 – 1.0 (Green et al. 2014). The ASKAP observations have revealed faint filamentary structures that were previously not visible, leading us to believe that it is actually three separate overlapping sources. As shown in Fig. B2, there are two brighter, elliptically shaped sources, one located to the north-west (G323.6 – 0.8) and the other to the south-east (G323.9 – 1.1). The third source (G323.6 – 1.1) appears to lie behind the other two sources and only a faint south-western edge can be seen. Because this source is very faint and overlaps with the other sources, it was not possible to obtain a flux estimate. For the two brighter sources, only rough upper limits could be obtained for the flux densities. It is

unclear if all three sources are SNRs but none of them has an obvious MIR counterpart.

#### 4.1.3 $G323.7 + 0.0$

The source shown in Fig. B3 is a small shell-like structure that is roughly circular and brightest along the southern edge. There is a small amount of overlap with a known H II region in the south-east and a larger H II region can be seen to the north-east. There is some faint MIR emission to the east that could be related to the radio emission. Since the emission is faint and the relation is not entirely clear, we include the source in our list of candidates.

#### 4.1.4 $G324.1 - 0.2$

This candidate does not have a clear shell-structure but it has a roughly circular shape with well-defined rounded edges, characteristic of a shock front (Fig. B4). There are several overlapping point sources and a bright H II region can be seen in the north-west. There is no clear MIR counterpart.

#### 4.1.5 $G324.1 + 0.0$

This source was originally identified as an SNR candidate by Whiteoak & Green (1996) but an image was not included. Green et al. (2014) have also listed it as a candidate and provided an image but there was insufficient evidence for it to be included in the Green (2022) catalogue. The source, seen in Fig. B5, is an elliptical shell, elongated in the east–west direction, with the brightest emission coming from the north and a fainter shell visible in the south. Multiple H II regions can be seen in the image and there is some overlap between the SNR candidate and H II regions in the north-west and north-east. This candidate is visible in the GLEAM data and a spectral index of  $-0.3 \pm 0.2$  was determined. The index indicates the emission may be non-thermal but the uncertainty is too large to be conclusive. Because this source has been studied previously and has a very clear shell-like morphology, we believe it should be classified as an SNR.

#### 4.1.6 $G324.3 + 0.2$

The source shown in Fig. B6 has a shell structure that is almost perfectly circular, with some brightening towards the south-east. Based on the distinct morphology and clear lack of an MIR counterpart, we believe this candidate should be classified as an SNR. A large, bright H II region can be seen to the west of the source.

#### 4.1.7 $G324.4 - 0.4$

In Fig. B7, we see an elliptical shell with brightening along the south-west edge. There are many overlapping point sources and a couple of known H II regions located to the north-east. There is overlapping emission in the MIR but nothing that clearly mirrors the shell structure seen in the radio.

#### 4.1.8 $G324.4 - 0.2$

The source shown in Fig. B8 is a very small, faint shell-like structure with an overlapping point source. It is located just north of  $G324.4 - 0.4$  and can also be seen in Fig. B7. There is no obvious MIR counterpart.

#### 4.1.9 $G324.7 + 0.0$

This candidate is a partial shell that arcs in the southern direction with no clear northern counterpart though some faint emission can be seen extending north from the southern shell (Fig. B9). There is a bright overlapping point source in the east. Several bright point sources can be seen in the MIR but the shell has no counterpart.

#### 4.1.10 $G324.8 - 0.1$

As shown in Fig. B10, this source consists of faint filaments that form a large ellipse. The source overlaps with  $G324.7 + 0.0$  and with a large H II region in the north-east. Because of this overlap, only a rough upper limit could be obtained for the flux. The rounded filaments do not appear to have an MIR counterpart.

#### 4.1.11 $G325.0 - 0.5$

This candidate, shown in Fig. B11, is composed of filaments that form a roughly elliptical structure. Many overlapping sources can be seen, including  $G325.0 - 0.3$  and several H II regions. A long filament, which can be seen in MIR and is thus likely thermal, runs from the north-east to the south-west. The filaments that form the edges of the ellipse are not visible in MIR. Because of the overlapping emission, only an upper limit could be obtained for the flux.

#### 4.1.12 $G325.0 - 0.3$

This candidate was originally identified by Whiteoak & Green (1996) (with no image) and later studied by Green et al. (2014) who provided an image but the source is not included in the Green (2022) catalogue. In Fig. B12, a clear shell structure can be seen that is brightest to the east. A filament of emission can be seen to the east of the candidate but it is likely thermal and unrelated. The candidate has no MIR counterpart. Based on our observations and the previous studies, we believe this source should be classified as an SNR.

#### 4.1.13 $G325.0 + 0.2$

This source consists of roughly circular emission that is brightened to the west where the edge of the source is the most well-defined (Fig. B13). A bright overlapping point source can be seen to the east. Emission can be seen in the MIR but it does not have the same rounded structure as the radio source.

#### 4.1.14 $G325.8 - 2.1$

This object is composed of very faint filaments of emission found to the south-west of the bright known SNR  $G326.3 - 1.8$ . As shown in Fig. B14 the source overlaps with negative bowls of emission, likely caused by missing short spacings. The filaments can be seen most clearly in the south-east but some faint structures are also visible in the north-west. This source is only visible because it is located at a far distance from the Galactic plane and there is little thermal emission. The source was too faint to obtain an estimate of the flux density.



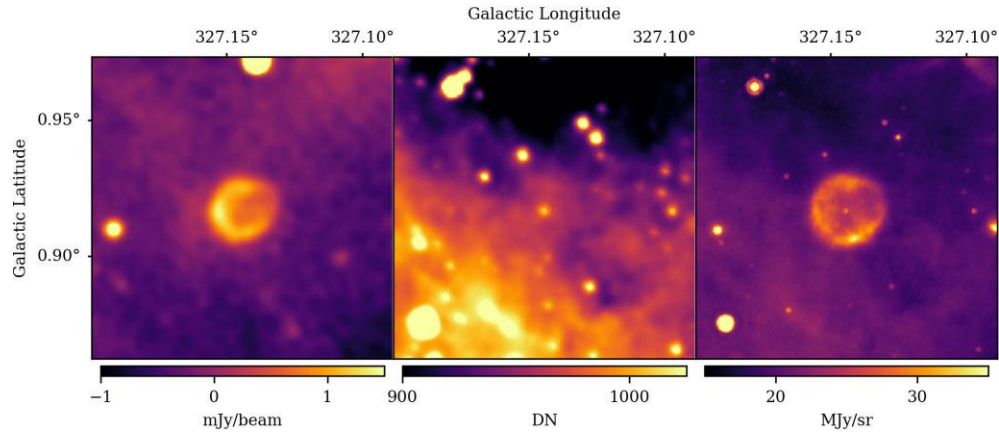


**Figure 9.** 933 MHz ASKAP data, 12  $\mu\text{m}$  WISE data, and 24  $\mu\text{m}$  MIPS data for G327.1 + 0.9.

#### 4.1.15 G325.8 + 0.3

This candidate is composed of rounded filamentary structures that can be seen to the north and south-east in Fig. B15. The source overlaps with a large H II region and many point sources. Missing short interferometer spacings generate a negative bowl around these strong emitters. Because of this, and because the filaments are so faint, we were unable to obtain a flux estimate for the source.

#### 4.1.16 G327.1 + 0.9

This candidate is a small, roughly circular source that appears to have a brightened shell-like edge to the east (Fig. B16). This is our smallest source with a size of  $2'$  and we believe that this marks the approximate lower size limit of sources in which we would be able to detect a shell-like structure, given the resolution of our data. This source appears in Gvaramadze, Kniazev & Fabrika (2010) in their table of 24  $\mu\text{m}$  nebulae compiled using data from the Multiband Imaging Photometer for Spitzer (MIPS). There is a circular MIR nebula at 24  $\mu\text{m}$  (diameter of  $1.6'$ ) with a total flux of 1.4 Jy (Mizuno et al. 2010), with a compact source in the infrared visible at the centre. Since there is no counterpart at the WISE 12  $\mu\text{m}$  image (see Fig. 9,  $F_{12} < 0.05$  Jy), the source meets our criteria for a candidate. However, Gvaramadze et al. (2010) identify this source as a possible wind driven bubble around a Wolf-Rayet (WR) star. The dusty nebulae around WR stars can be bright at 22  $\mu\text{m}$  and relatively faint at  $\sim 12$   $\mu\text{m}$ , with spectroscopy studies suggesting that most emission toward WR nebulae at  $\sim 12$   $\mu\text{m}$  comes from material along the line of sight (e.g. Toalá et al. 2015). Since the winds from Wolf-Rayet stars can be detected in the 1.4-GHz radio continuum (e.g. Güdel 2002), this candidate could be a dusty WR nebula. However, G327.1 + 0.9 is an extended shell-like radio source and the radio emission from Wolf-Rayet winds is typically centrally peaked and does not extend much further than 1000 stellar radii (Güdel 2002). In this case, we propose that there are three possible explanations for G327.1 + 0.9. The first would be a late stage H II region produced by the central Wolf-Rayet star. The second would be a planetary nebula (Ingallinera et al. 2016). Finally, it could be the SNR of a supernova that exploded in a binary system. Follow-up polarimetric observations at high radio frequencies with ATCA should help to solve this mystery, as only the SNR would show linearly polarized radio emission.

#### 4.1.17 G328.0 + 0.7

The source shown in Fig. B17 is composed of roughly circular emission with a well-defined edge that is brightest in the northern part of the shell. There is a point source located near the centre of the candidate that coincides with the location of the known young ( $\sim 37$  kyrs) pulsar J1551 – 5310 (Hobbs et al. 2004; Manchester et al. 2005). Several H II regions can be seen in the south. There is possibly polarization associated with the north-west edge of the shell but it cannot be definitely differentiated from the background emission, as shown in Fig. 10. We do see clear polarization coming from the central pulsar with a RM of  $-1017 \pm 5$   $\text{rad m}^{-2}$ , consistent with the catalogued value of  $-1023.3 \pm 6.3$   $\text{rad m}^{-2}$  (Han et al. 2018). Because of the possible association with a young pulsar and detectable polarization, we believe this source should be classified as a SNR.

#### 4.1.18 G328.6 + 0.0

This source was observed by McClure-Griffiths et al. (2001) and is listed by Green (2022) as an SNR candidate but it does not appear in the actual catalogue. Here, we see elongated filaments that form a roughly elliptical shape, which could be two separate sources (Fig. B18). There is a well-defined shell-like edge in the south-west and less defined shell-like filaments in the north-east. There are several overlapping H II regions and an unidentified bright point source located near the geometric centre of the south-west arc that may be polarized. The very bright source to the north-west of the image is G328.4 + 0.2. This source is visible in the GLEAM data and a steep negative spectral index of  $-0.75 \pm 0.06$  was determined, indicating the emission is likely non-thermal. We believe this source should also be classified as a SNR.

#### 4.1.19 G330.2 – 1.6

This source, shown in Fig. B19, is very faint but it is located at a far distance from the Galactic plane making it detectable. It has a clear circular shell-like structure with little to no emission coming from the centre and no obvious MIR counterpart. The filamentary emission seen in the south-east appears to be unrelated and may instead be a radio galaxy, with a bright core, two external bright spots, and internal lobes, indicating jet precession.

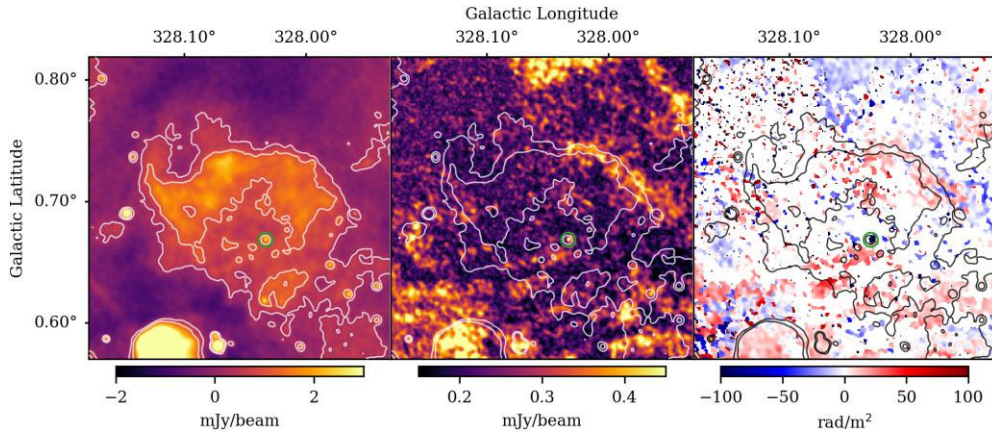


**Figure 10.** Total power, PI, and RM maps for G328.0 + 0.7 with total power contours to indicate where emission overlaps. The green circle indicates the location of the young pulsar, which is polarized and has a high RM.

## 5 DISCUSSION

### 5.1 Estimating the SNR density of the Galactic disc

Based on our estimate of the size of the Galactic SNR population, we can roughly estimate the theoretical SNR surface density of the Galactic disc. Since most SNRs should be found within the star-forming disc, we assume a Galactic radius of 12.5 kpc, which encompasses 95 percent of the stellar mass of the Milky Way disc (Binney & Vasiliev 2023). We estimate that the Milky Way should have at least 1000–2700 radio-bright SNRs. This corresponds to an average Galactic SNR surface density between 2.0 and 5.5 SNRs  $\text{kpc}^{-2}$ . We can compare this range of values to the density of known Galactic SNRs. The University of Manitoba’s SNRcat (Ferrand & Safi-Harb 2012) currently lists 383 SNRs and SNR candidates. Of these, 369 have been detected in the radio. Thus, the Galaxy has an average known SNR surface density of only 0.75 radio-bright SNRs  $\text{kpc}^{-2}$ .

To gain further insight into the missing SNR population, we can analyse how the known SNRs are distributed within the Galaxy by quadrant. Quadrants I and IV look towards the Galactic centre and encompass a larger, but denser, part of the Galactic plane. Quadrants II and III look away from the Galactic centre with shorter lines of sight and less emission. The known SNR surface density distribution can be broken down by quadrant as follows:

- (i) Quadrant I ( $0^\circ \leq l < 90^\circ$ ): 0.74 SNRs  $\text{kpc}^{-2}$
- (ii) Quadrant II ( $90^\circ \leq l < 180^\circ$ ): 1.23 SNRs  $\text{kpc}^{-2}$
- (iii) Quadrant III ( $180^\circ \leq l < 270^\circ$ ): 0.63 SNRs  $\text{kpc}^{-2}$
- (iv) Quadrant IV ( $270^\circ \leq l < 360^\circ$ ): 0.72 SNRs  $\text{kpc}^{-2}$

We see that Quadrant II has a noticeably higher density of known SNRs than the other quadrants. It is likely higher than Quadrants I and IV because SNRs in Quadrant II are closer (on average) and there is less thermal emission in this direction. Quadrant II is also relatively well-surveyed which may explain why it has a higher density of known SNRs than Quadrant III.

The EMU/POSSUM Galactic pilot II field ( $323^\circ \leq l < 330^\circ$ ) has seven known SNRs giving it an SNR surface density of 0.34 SNRs  $\text{kpc}^{-2}$ , around a factor of 2 lower than the Quadrant IV average. To achieve the theoretical average Galactic SNR density of 2.0–5.5 SNRs  $\text{kpc}^{-2}$ , we would need to find 34–106 new SNRs in this field. If we include our 21 SNR candidates, the density of known SNRs

is brought up to 1.36 SNRs  $\text{kpc}^{-2}$ , which is comparable to the SNR density we see in Quadrant II.

### 5.2 The known Galactic SNR population

Fig. 11 shows how the angular sizes and flux densities of our SNR candidates compare to the known Galactic SNR population, not including the candidates for which we were unable to determine a reliable flux density. This plot was made using data from Green (2022), omitting sources where no flux estimate was given. It should be noted that 1 GHz flux densities are provided in Green’s catalogue and our 933 MHz values were not adjusted to this frequency since we do not have spectral indices for most of the candidates. However, given the small frequency difference relative to the scale of the plot, the changes in the positions of the points are insignificant, even for sources with steep spectra.

The shaded regions of the plot indicate what we estimate to be the limits of what can be detected with our data. The minimum size was chosen to be  $2'$  as this is the size of our smallest source and we believe it would be difficult to detect shell-like structures for smaller sources given the  $18'$  resolution. The minimum surface brightness was based on an estimate of the minimal thermal noise (taken to be  $\sigma = 40 \mu\text{Jy beam}^{-1}$ ), though variations across the image likely set different limits for different regions. The grey dotted lines in the plot represent the  $\sigma$  and  $3\sigma$  surface brightness limits. Because we are studying extended sources, rather than point sources, we are able to detect sources below the theoretical thermal noise limit.

Our results support that there is likely still a large population of undetected SNRs within our Galaxy. Fig. 11 demonstrates that many of our candidates are smaller and fainter than most known SNRs. This may be evidence that some of the missing SNR population was missing because it was previously undetectable. Improvements in the angular resolution and sensitivity of radio telescopes should then allow for the detection of some of these SNRs in future sky surveys. It may be that improvements in angular resolution are more important as the technological surface brightness lower limit is approaching the limit set by the background emission (Anderson et al. 2017; Dokara et al. 2023). However, future improvements in angular resolution may also have limited impact in Galactic SNR observations. Given that we have shown we are capable of detecting shell-like structures in sources as small as  $2'$ , even at the farthest Galactic distances within this field ( $\sim 18$  kpc) we should be able to detect sources with linear sizes as small as 10 pc. Based on observations of other Local Group

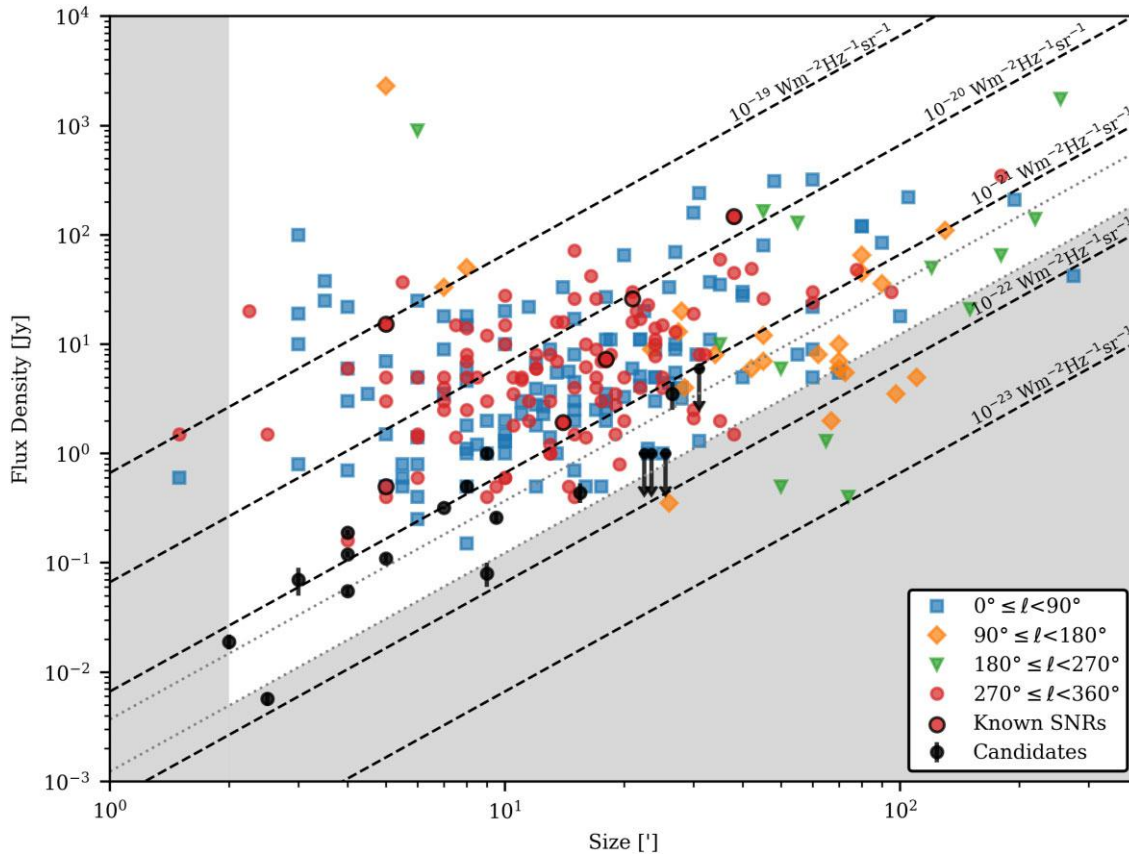


**Figure 11.** Sizes and flux densities of our SNR candidates compared with the known SNR population as a function of quadrant [data from Green (2022), sources without flux estimates omitted]. The ‘Known SNRs’ are the six SNRs that are fully imaged in our field. The ‘Candidates’ are the 18 SNR candidates listed in this paper for which we were able to obtain flux estimates. Note that for some candidates the error bars are too small to be visible and others have arrows to indicate that the values should be taken as upper limits. The dashed lines are lines of constant surface brightness. Shaded regions indicate the approximate limits of what we believe we should be able to detect with ASKAP at this frequency. The grey dotted lines represent the  $\sigma$  and  $3\sigma$  thermal noise limits.

galaxies (Badenes, Maoz & Draine 2010; Long et al. 2010) and given that X-ray observations of young (small) Galactic SNRs are believed to be fairly complete (Leahy et al. 2020), it is unlikely that there are many undetected sources below this size limit. Thus, any remaining missing SNRs in this field are most likely obscured by superimposed radio-bright sources, particularly H II regions.

The impact of background emission on SNR detection can be further demonstrated by the fact that we were not able to detect new sources in the brighter part of the field that we believe to be associated with the Norma arm. In fact, almost all of our candidates are in the lower right corner of the field, as shown in Fig. 3. Theoretically, there should be a higher density of SNRs within and near spiral arms. If we compare the bright upper left half of the image to the lower right half, including our candidates the former has an SNR density of  $\sim 1$  SNR  $\text{kpc}^{-2}$  while the latter has a density of  $\sim 2$  SNRs  $\text{kpc}^{-2}$ , which is the theoretical lower limit we derived in Section 5.1. While the actual SNR density should be higher in the upper left half, we find the observed SNR density to be higher in the lower right half. This indicates there is likely still a population of SNRs within the bright part of the field that we were unable to detect. Further, this demonstrates the impact of background emission in setting detectability limits and supports that technological improvements in sensitivity may no longer be as effective for detecting new radio SNRs in these types of regions.

## 6 CONCLUSIONS

In this paper, we used pilot data from ASKAP to study the known SNR population in a small field of the Galactic plane. We also found 21 SNR candidates, three times the number of known SNRs in this field. Of the candidates, 13 have not been previously studied, four have been studied as SNR candidates, three classed as a single SNR, and one studied as an MIR nebula. For most candidates, observations at a second, ideally higher, frequency are required to confirm the sources as SNRs as these observations would likely provide more information about polarization and spectral indices.

The results of this paper demonstrate the potential for the full EMU/POSSUM surveys, taking place over the next few years, to fill in some of the missing Galactic SNR population through the detection of small and/or faint sources. We were able to detect sources that seem to have been missed in previous surveys due to their small angular size and/or low surface brightness. Comparing the properties of our candidates to the known Galactic SNR population further supports this. Future work using ASKAP data to expand upon the size of the surveyed Galactic field will likely detect more of these types of sources, allowing for a better characterization of the Galactic SNR population. In this field, we have uncovered approximately 1 new SNR  $\text{kpc}^{-2}$ . The full EMU/POSSUM surveys will cover roughly 60 per cent of the Galactic plane meaning they could hypothetically uncover around 300 new SNRs. However, it is important to note the impact of background emission and the challenges we faced in



detecting low surface brightness SNRs in complex regions. Because a significant portion of the surveyed area will be in the direction of the Galactic centre, it is unlikely that we will be as successful in these denser, brighter fields.

The missing SNR problem and the size of the Galactic SNR population remain difficult problems to exactly quantify. While technological advancements have continued to lead to new SNR detections, there is likely a population of SNRs that will never be observed due to detection limits set by the local background. Estimates of the size of the Galactic SNR discrepancy should then exclude these types of sources as they may be considered undetectable. In future work we hope to further explore this problem, utilizing the full EMU/POSSUM surveys to study variations in SNR detectability across the Galactic plane.

## ACKNOWLEDGEMENTS

We are grateful to an anonymous referee whose comments improved the quality of the paper. This scientific work uses data obtained from Inyarrimanha Ilgari Bundara/the Murchison Radio-astronomy Observatory. We acknowledge the Wajarri Yamaji People as the Traditional Owners and native title holders of the Observatory site. CSIRO's ASKAP radio telescope is part of the Australia Telescope National Facility (<https://ror.org/05qajvd42>). Operation of ASKAP is funded by the Australian Government with support from the National Collaborative Research Infrastructure Strategy. ASKAP uses the resources of the Pawsey Supercomputing Research Centre. Establishment of ASKAP, Inyarrimanha Ilgari Bundara, the CSIRO Murchison Radio-astronomy Observatory, and the Pawsey Supercomputing Research Centre are initiatives of the Australian Government, with support from the Government of Western Australia and the Science and Industry Endowment Fund. The POSSUM project (<https://possum-survey.org>) has been made possible through funding from the Australian Research Council, the Natural Sciences and Engineering Research Council of Canada (NSERC), the Canada Research Chairs Program, and the Canada Foundation for Innovation. This publication makes use of data products from the Wide-field Infrared Survey Explorer, which is a joint project of the University of California, Los Angeles, and the Jet Propulsion Laboratory/California Institute of Technology, funded by the National Aeronautics and Space Administration. RK acknowledges the support of NSERC, funding reference number RGPIN-2020-04853. ER acknowledges the support of NSERC, funding reference number RGPIN-2022-03499. The Dunlap Institute is funded through an endowment established by the David Dunlap family and the University of Toronto. BMG acknowledges the support of NSERC through grant RGPIN-2022-03163, and of the Canada Research Chairs program. DL acknowledges the support of NSERC.

## DATA AVAILABILITY

ASKAP data are available on the CSIRO ASKAP Science Data Archive (CASDA) (<https://research.csiro.au/casda/>)

## REFERENCES

- Albert C., Dwarkadas V. V., 2022, *MNRAS*, 514, 728
- Anderson L. D., Bania T. M., Balsa D. S., Cunningham V., Wenger T. V., Johnstone B. M., Armentrout W. P., 2014, *ApJS*, 212, 1
- Anderson L. D. et al., 2017, *A&A*, 605, A58
- Badenes C., Maoz D., Draine B. T., 2010, *MNRAS*, 407, 1301
- Bell A. R., 1978, *MNRAS*, 182, 147
- Bianchi S., Schneider R., 2007, *MNRAS*, 378, 973
- Binney J., Vasiliev E., 2023, *MNRAS*, 520, 1832
- Blandford R. D., Ostriker J. P., 1978, *ApJ*, 221, L29
- Brogan C. L., Gelfand J. D., Gaensler B. M., Kassim N. E., Lazio T. J. W., 2006, *ApJ*, 639, L25
- Camilo F., Ransom S. M., Halpern J. P., Reynolds J., 2007, *ApJ*, 666, L93
- Camilo F., Reynolds J., Johnston S., Halpern J. P., Ransom S. M., 2008, *ApJ*, 679, 681
- Clark D. H., Caswell J. L., Green A. J., 1975, *Australian Journal of Physics Astrophysical Supplement*, 37, 1
- Comrie A. et al., 2021, CARTA: The Cube Analysis and Rendering Tool for Astronomy, Astrophysics Source Code Library, record ascl:2103.031
- Cutri R. M. et al., 2003, *VizieR Online Data Catalog*, p. II/246
- Cutri R. M. et al., 2013, Explanatory Supplement to the AllWISE Data Release Products, WISE
- Dickel J. R., Milne D. K., Strom R. G., 2000, *ApJ*, 543, 840
- Dokara R. et al., 2018, *ApJ*, 866, 61
- Dokara R. et al., 2021, *A&A*, 651, A86
- Dokara R. et al., 2023, *A&A*, 671, A145
- Draine B. T., 2011, *Physics of the Interstellar and Intergalactic Medium*. Princeton Univ. Press, Princeton
- Dubner G., 2017, in Alsabti A. W., Murdin P. eds, *Handbook of Supernovae*. Springer, Berlin, p. 2041
- Dubner G., Giacani E., 2015, *A&A Rev.*, 23, 3
- Ferrand G., Safi-Harb S., 2012, *Adv. Space Res.*, 49, 1313
- Frail D. A., Goss W. M., Whiteoak J. B. Z., 1994, *ApJ*, 437, 781
- Fuerst E., Reich W., Sofue Y., 1987, *A&AS*, 71, 63
- Gaensler B. M., Dickel J. R., Green A. J., 2000, *ApJ*, 542, 380
- Gaensler B. M., Landecker T. L., Taylor A. R., *POSSUM Collaboration*, 2010, American Astronomical Society Meeting Abstracts #215. American Astronomical Society, Washington, p. 470.13
- Gelfand J. D., Gaensler B. M., 2007, *ApJ*, 667, 1111
- Gelfand J. D., Gaensler B. M., Slane P. O., Patnaude D. J., Hughes J. P., Camilo F., 2007, *ApJ*, 663, 468
- Goch R., 1995, in Shaw R. A., Payne H. E., Hayes J. J. E. eds, *ASP Conf. Ser. Vol. 77, Astronomical Data Analysis Software and Systems IV*. Astron. Soc. Pac., San Francisco, p. 144
- Green A. J., Reeves S. N., Murphy T., 2014, *PASA*, 31, e042
- Green D. A., 2015, *MNRAS*, 454, 1517
- Green D. A., 2019, *JA&A*, 40, 36
- Green D. A., 2022, A Catalogue of Galactic Supernova Remnants (2022 December version). Cavendish Laboratory, Cambridge, available at: <https://www.mrao.cam.ac.uk/surveys/snrs/index.html> (accessed 2023 January)
- Güdel M., 2002, *ARA&A*, 40, 217
- Gvaramadze V. V., Kniazev A. Y., Fabrika S., 2010, *MNRAS*, 405, 1047
- Han J. L., Manchester R. N., van Straten W., Demorest P., 2018, *ApJS*, 234, 11
- Helfand D. J., Becker R. H., White R. L., Fallon A., Tuttle S., 2006, *AJ*, 131, 2525
- Hobbs G. et al., 2004, *MNRAS*, 352, 1439
- Hotan A. W. et al., 2021, *PASA*, 38, e009
- Hurley-Walker N. et al., 2019, *PASA*, 36, e048
- Ingallinera A. et al., 2016, *MNRAS*, 463, 723
- Kothes R., 2017, in Torres D. F. ed., *Astrophysics and Space Science Library*, Vol. 446, Modelling Pulsar Wind Nebulae. Springer, Berlin, p. 1
- Kothes R., Brown J.-A., 2009, in Strassmeier K. G., Kosovichev A. G., Beckman J. E., eds, *Proc. IAU Symp. 259, Cosmic Magnetic Fields: From Planets, to Stars and Galaxies*. Cambridge Univ. Press, Cambridge, p. 75
- Kothes R., Reich W., 2001, *A&A*, 372, 627
- Kothes R., Reich P., Foster T. J., Reich W., 2017, *A&A*, 597, A116
- Leahy D. A., Ranasinghe S., Gelowitz M., 2020, *ApJS*, 248, 16
- Leahy D. A., Merrick F., Filipović M., 2022, *Universe*, 8, 653
- Long K. S. et al., 2010, *ApJS*, 187, 495
- McClure-Griffiths N. M., Green A. J., Dickey J. M., Gaensler B. M., Haynes R. F., Wieringa M. H., 2001, *ApJ*, 551, 394
- Manchester R. N., Hobbs G. B., Teoh A., Hobbs M., 2005, *AJ*, 129, 1993
- Mizuno D. R. et al., 2010, *AJ*, 139, 1542

Norris R. P. et al., 2011, *PASA*, 28, 215  
 Norris R. P. et al., 2021, *PASA*, 38, e046  
 Padmanabhan T., 2001, *Theoretical astrophysics, Vol. 2. Stars and Stellar Systems*. Cambridge Univ. Press, Cambridge  
 Pinheiro Gonçalves D., Noriega-Crespo A., Paladini R., Martin P. G., Carey S. J., 2011, *AJ*, 142, 47  
 Priestley F. D., Chawner H., Barlow M. J., De Looze I., Gomez H. L., Matsuura M., 2022, *MNRAS*, 516, 2314  
 Ranasinghe S., Leahy D., 2022, *ApJ*, 940, 63  
 Reynolds S. P., Gaensler B. M., Bocchino F., 2012, *Space Sci. Rev.*, 166, 231  
 Sarbadhicary S. K., Badenes C., Chomiuk L., Caprioli D., Huizenga D., 2017, *MNRAS*, 464, 2326  
 Slavin J. D., Dwek E., Jones A. P., 2015, *ApJ*, 803, 7  
 Sun M., Wang Z.-r., Chen Y., 1999, *ApJ*, 511, 274  
 Tammann G. A., Loeffler W., Schroeder A., 1994, *ApJS*, 92, 487  
 Tiengo A. et al., 2010, *ApJ*, 710, 227  
 Toalá J. A., Guerrero M. A., Ramos-Larios G., Guzmán V., 2015, *A&A*, 578, A66

Truelove J. K., McKee C. F., 1999, *ApJS*, 120, 299  
 van der Laan H., 1962, *MNRAS*, 124, 179  
 Wang S., Zhang C., Jiang B., Zhao H., Chen B., Chen X., Gao J., Liu J., 2020, *A&A*, 639, A72  
 Wayth R. B. et al., 2015, *PASA*, 32, e025  
 Whiteoak J. B. Z., Green A. J., 1996, *A&AS*, 118, 329  
 Whiteoak J. B., Gardner F. F., 1968, *ApJ*, 154, 807  
 Wright E. L. et al., 2010, *AJ*, 140, 1868

## APPENDIX A: KNOWN SNRS

In Figs A1–A6, we present images of the known SNRs in the EMU/POSSUM Galactic pilot II field. Here, we show the 933-MHz radio images from ASKAP, the same region in the MIR at  $12\ \mu\text{m}$  using data from WISE, and a composite image with radio emission shown in red and MIR in blue.

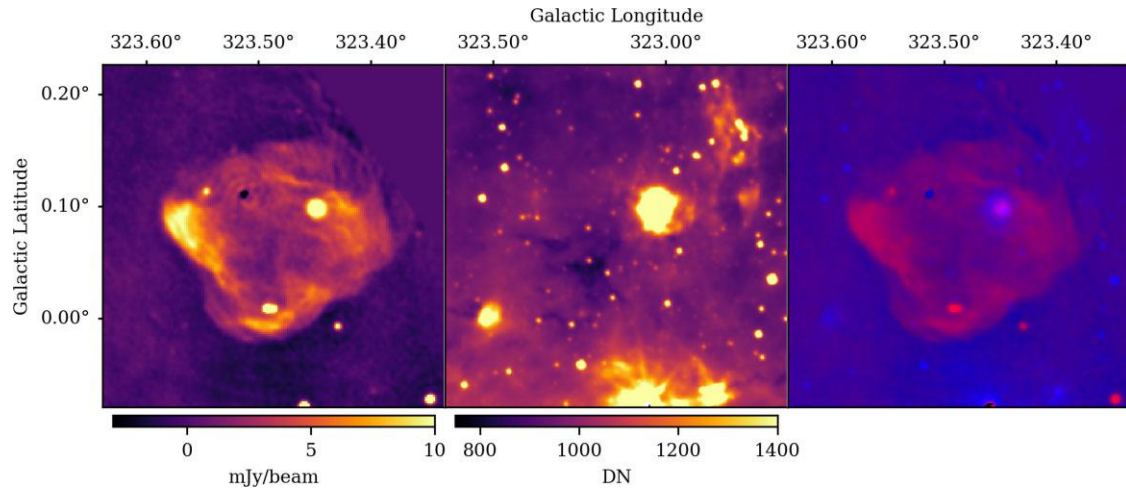


Figure A1. G323.5 + 0.1.

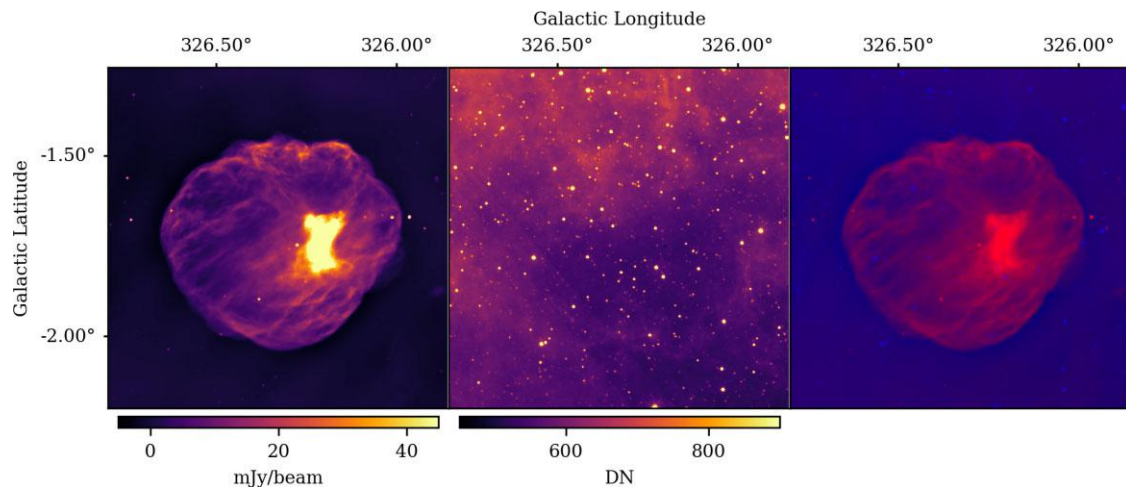


Figure A2. G326.3 - 1.8.

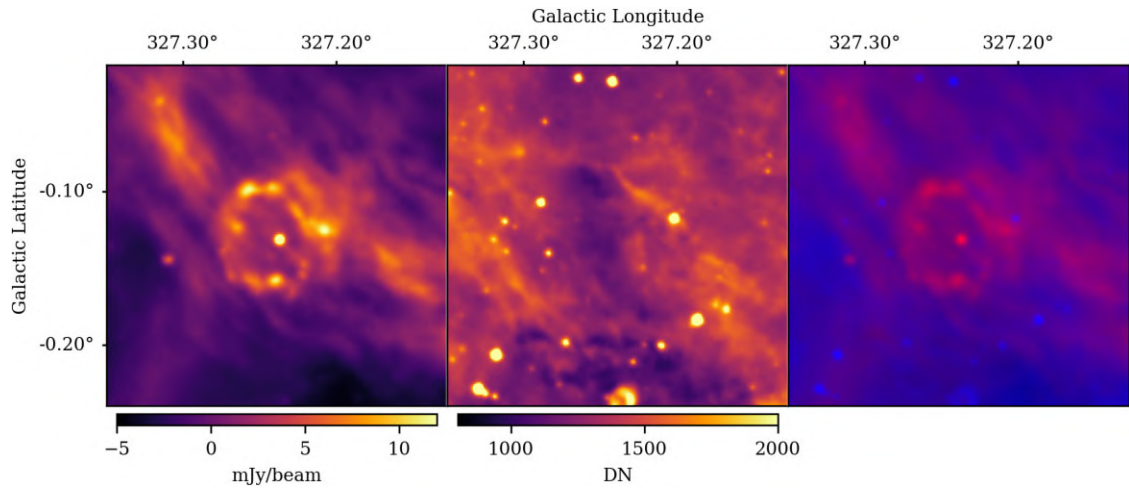


Figure A3. G327.2 - 0.1.

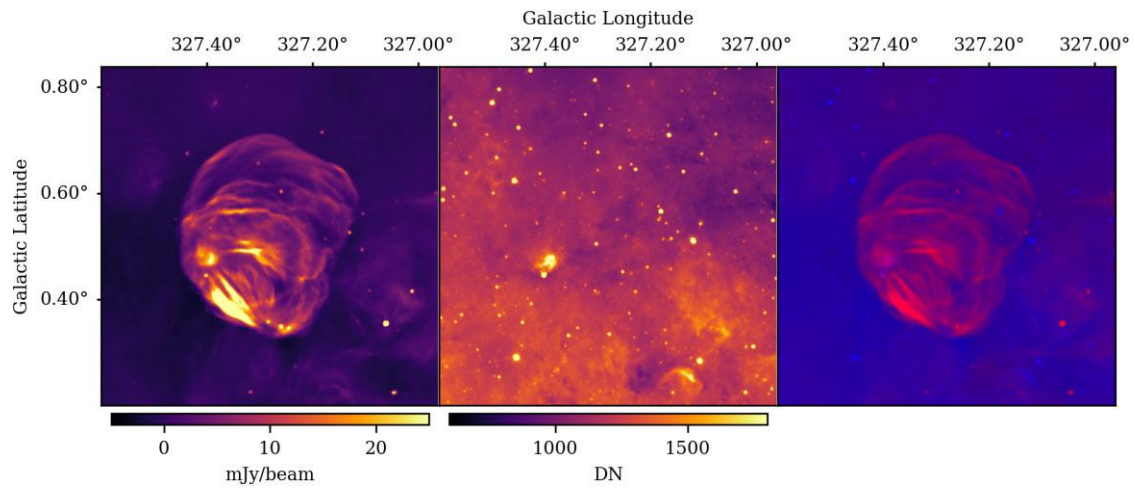


Figure A4. G327.4 + 0.4.

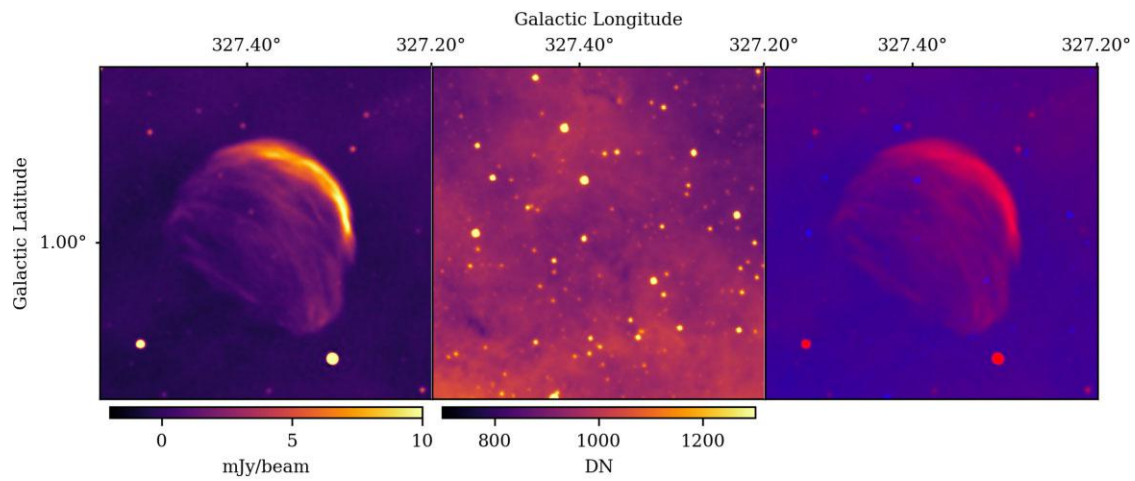


Figure A5. G327.4 + 1.0.



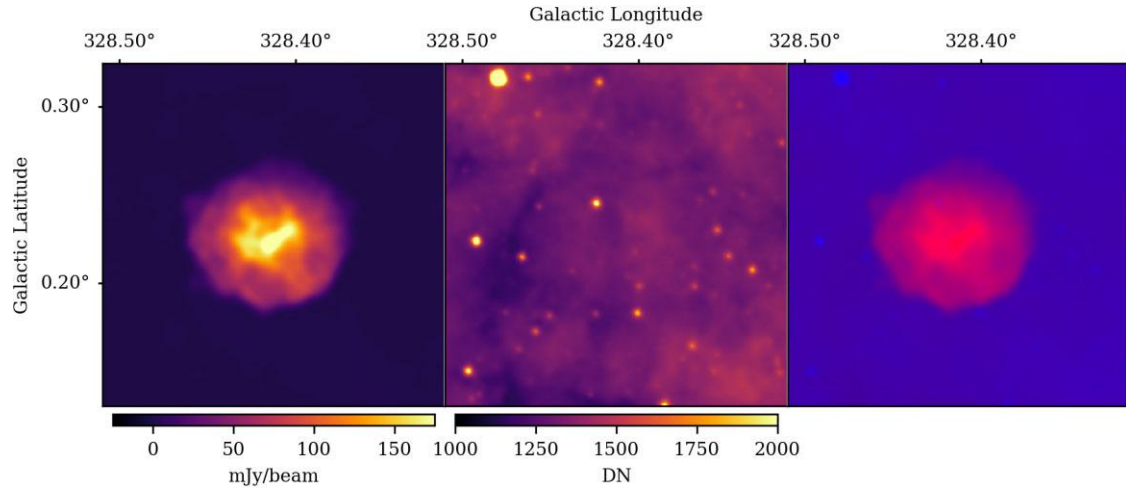


Figure A6. G328.4 + 0.2.

## APPENDIX B: SNR CANDIDATES

In Figs B1–B19, we present images of the SNR candidates in the EMU/POSSUM Galactic pilot II field using the same format

described in Appendix A. These are sources that do not appear in the Green (2022) radio SNR catalogue.

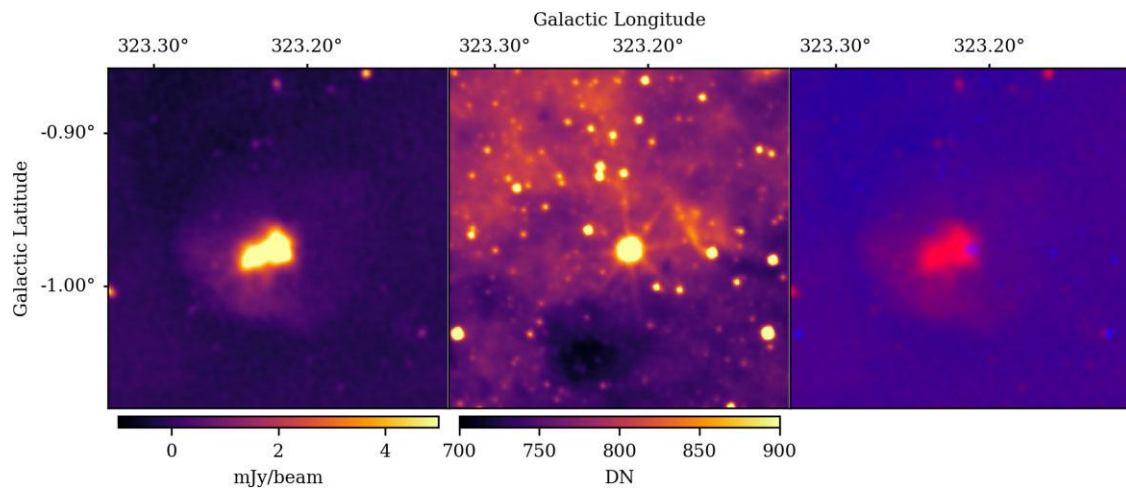
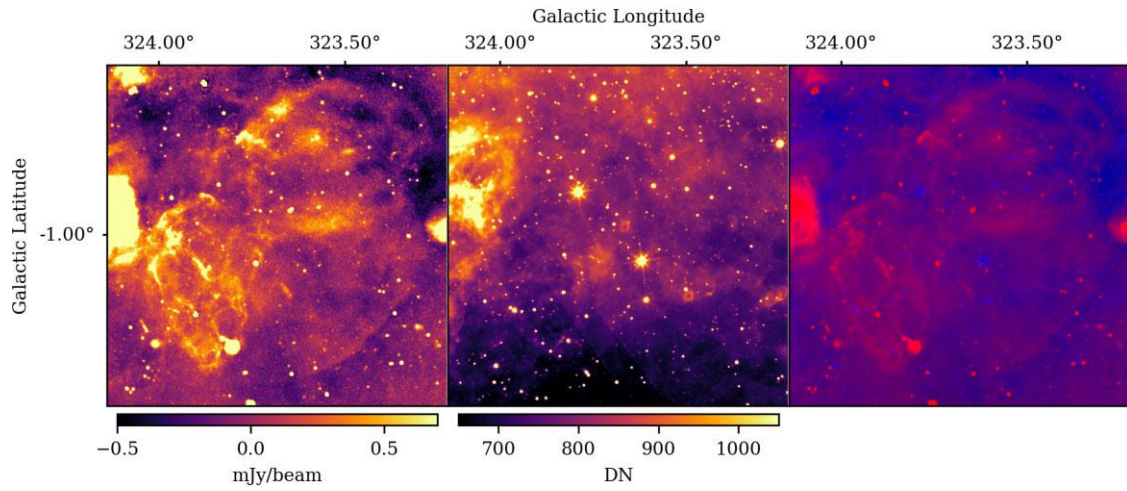
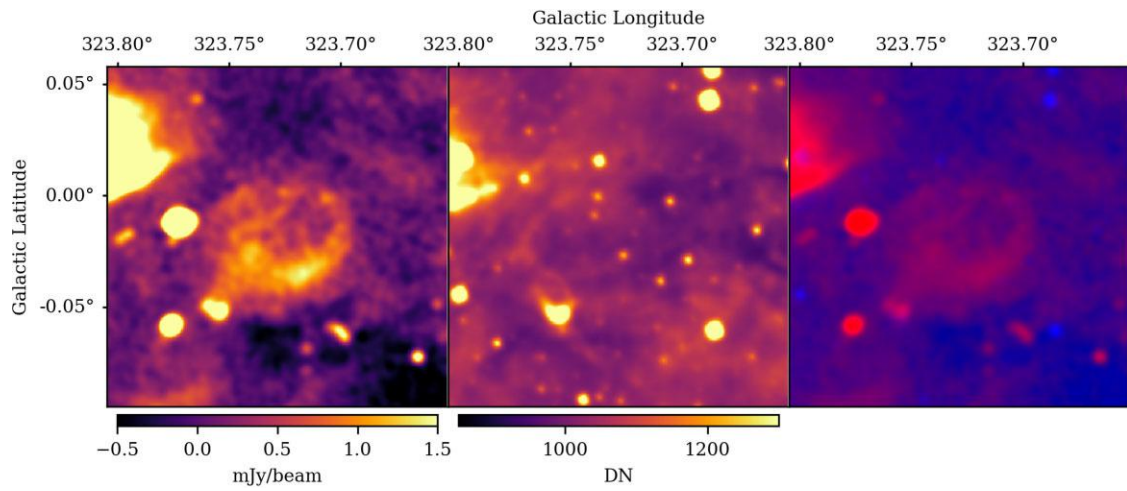


Figure B1. G323.2 - 1.0.



**Figure B2.** G323.6 – 1.1, G323.6 – 0.8, and G323.9 – 1.1.



**Figure B3.** G323.7 + 0.0.

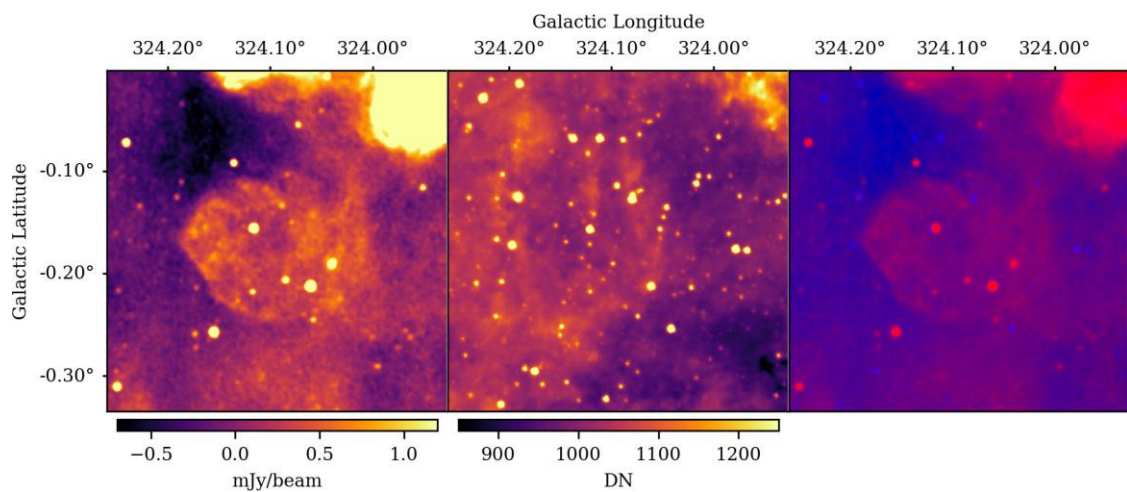


**Figure B4.** G324.1 – 0.2.

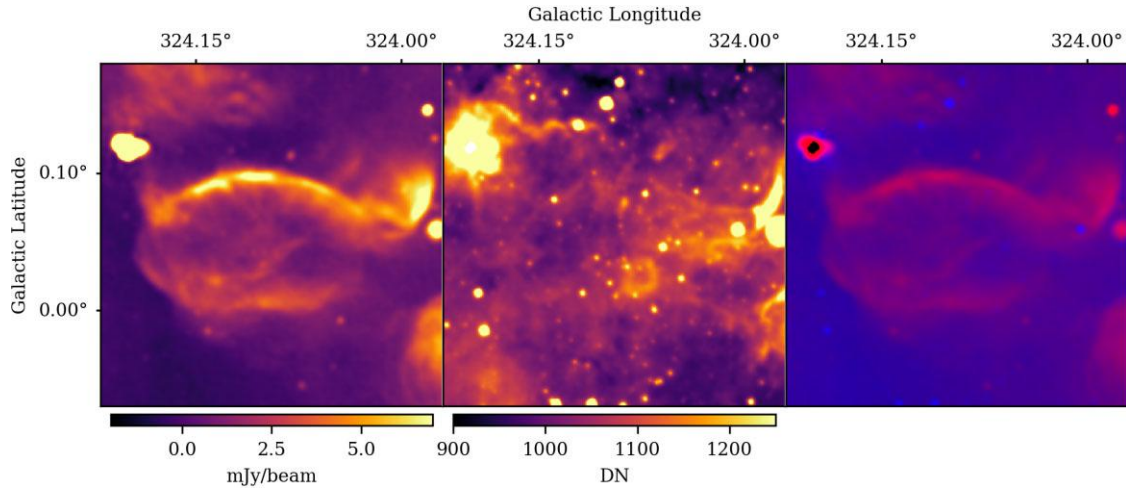


Figure B5. G324.1 + 0.0.

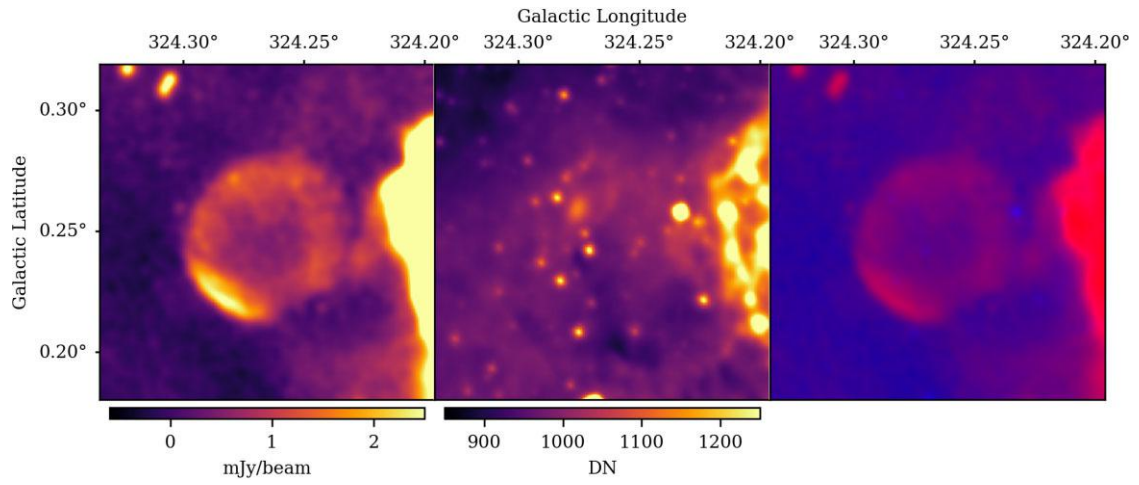


Figure B6. G324.3 + 0.2.

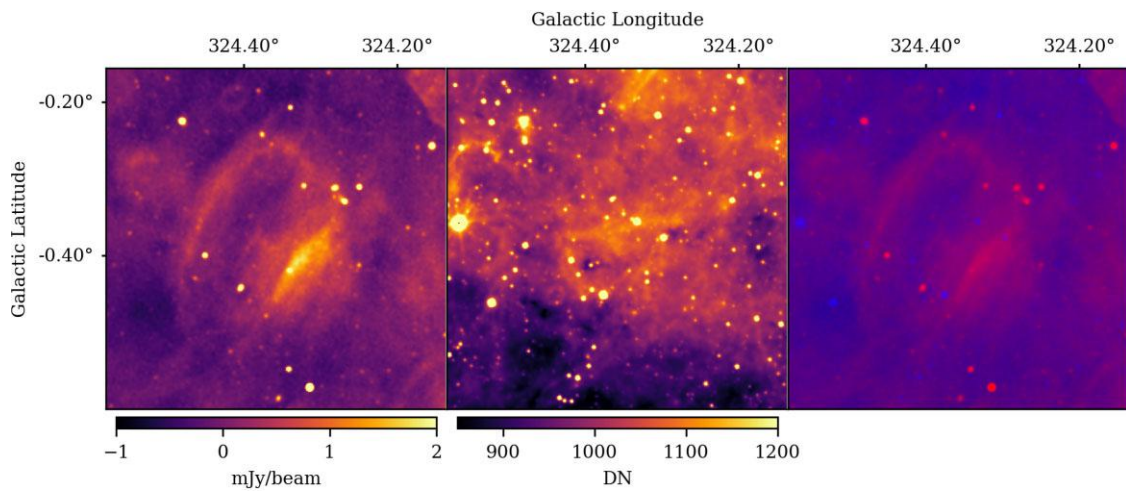
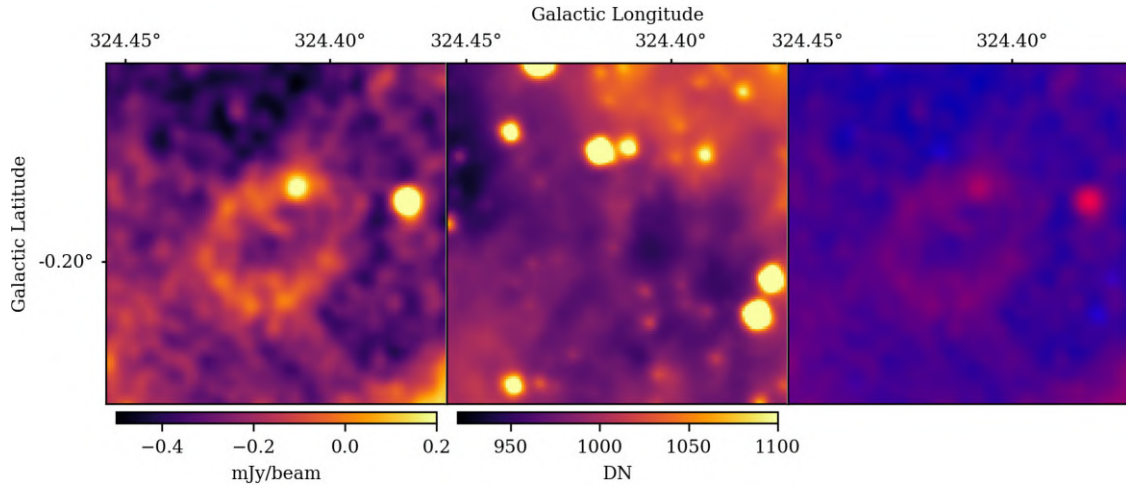
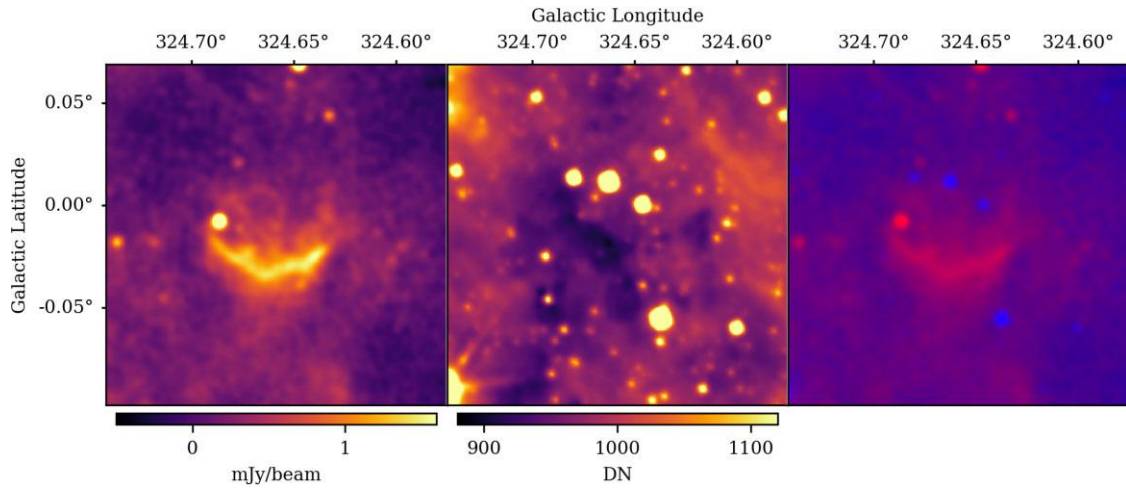


Figure B7. G324.4 - 0.4.





**Figure B8.** G324.4 – 0.2.



**Figure B9.** G324.7 + 0.0.

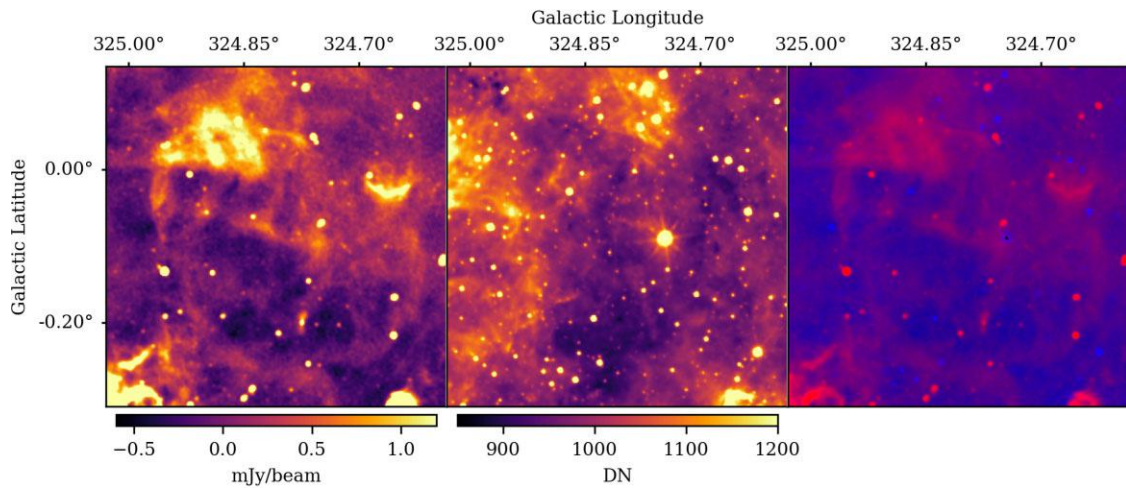


**Figure B10.** G324.8 – 0.1.

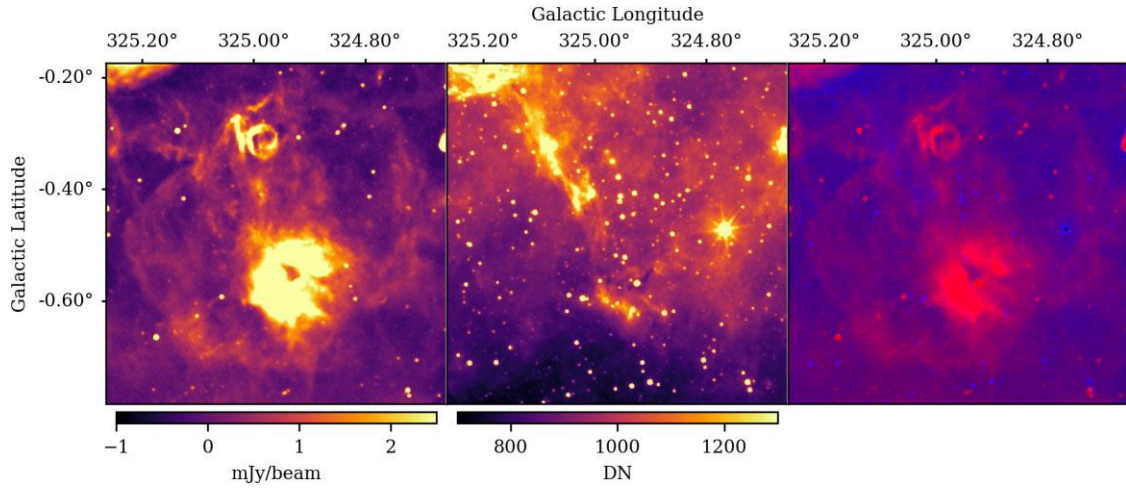


Figure B11. G325.0 – 0.5.

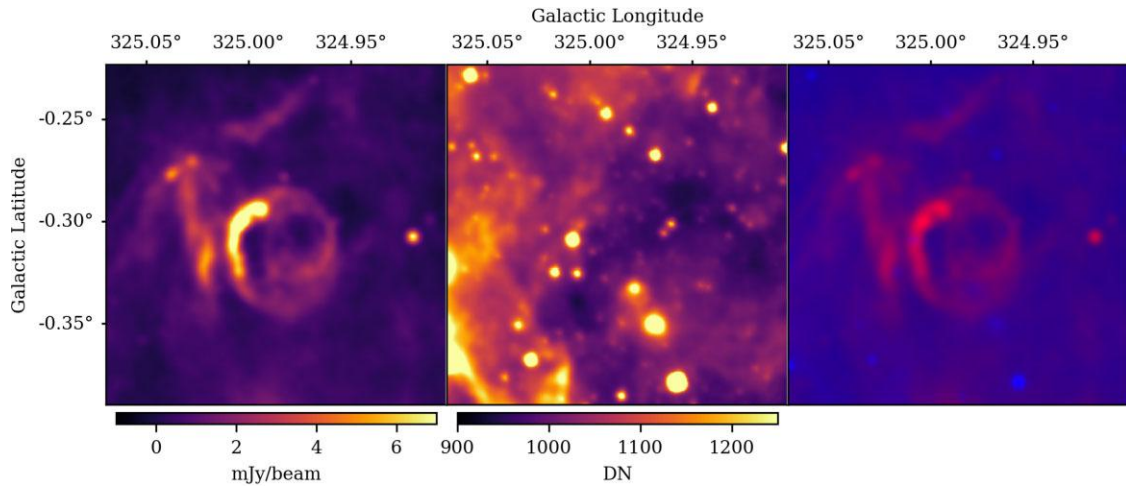


Figure B12. G325.0 – 0.3.

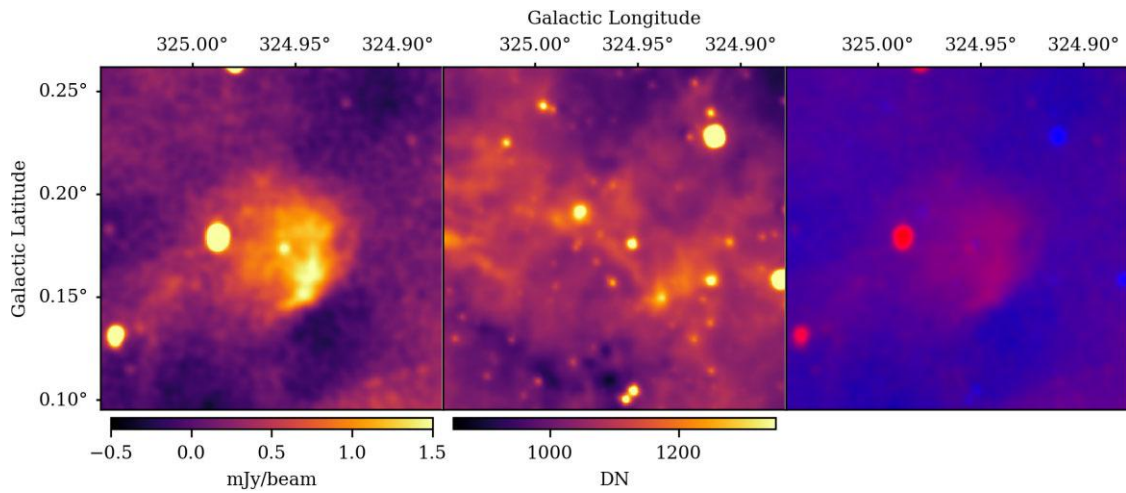


Figure B13. G325.0 + 0.2.



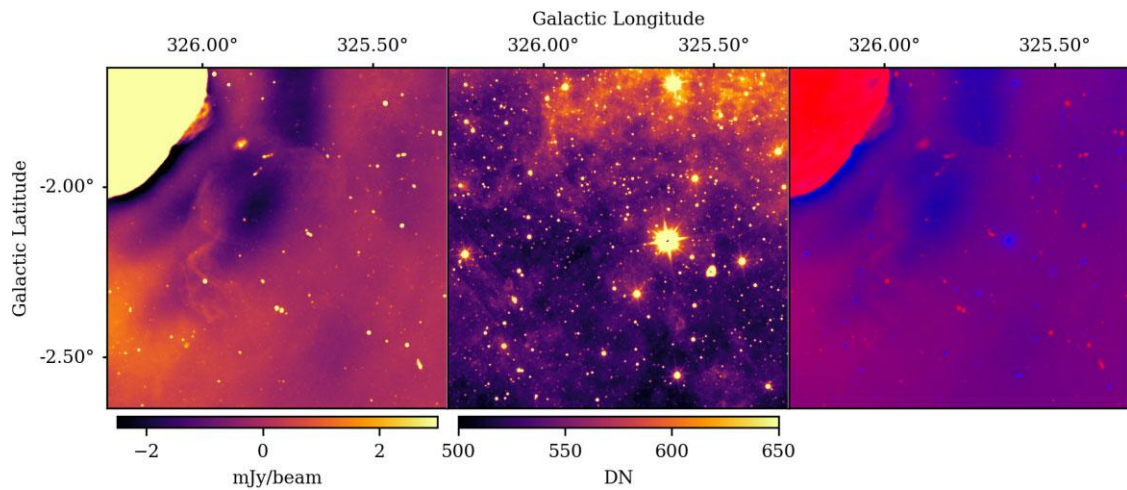


Figure B14. G325.8 - 2.1.

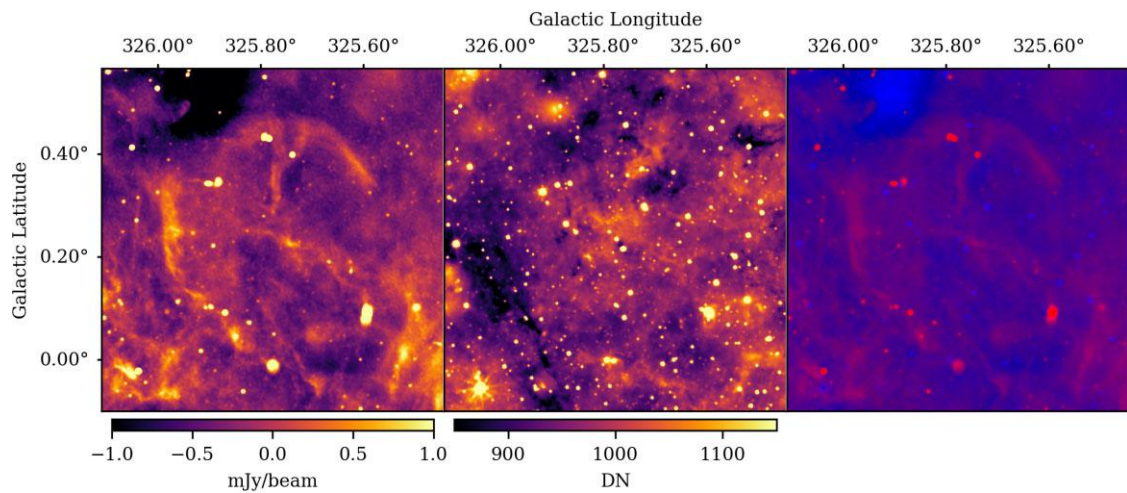


Figure B15. G325.8 + 0.3.

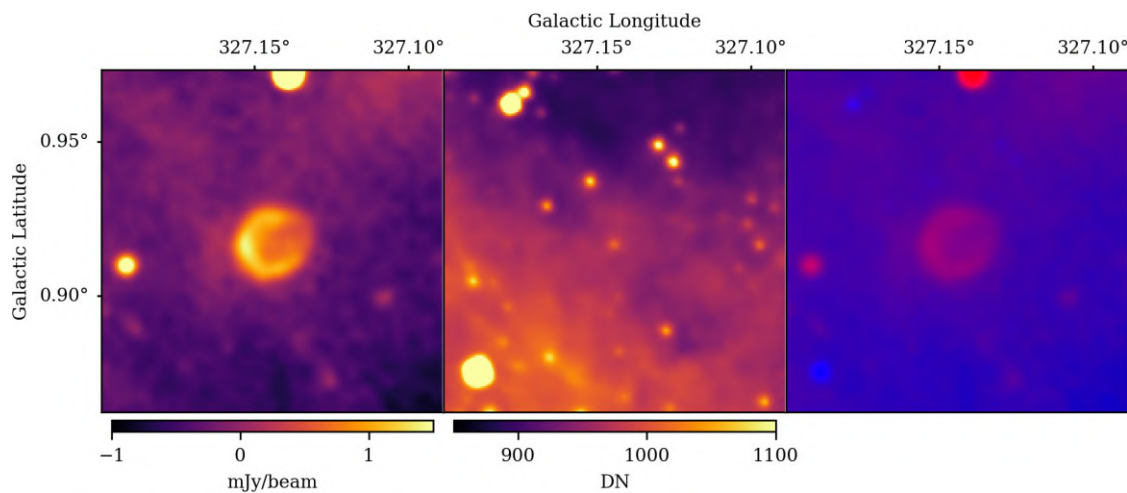


Figure B16. G327.1 + 0.9.



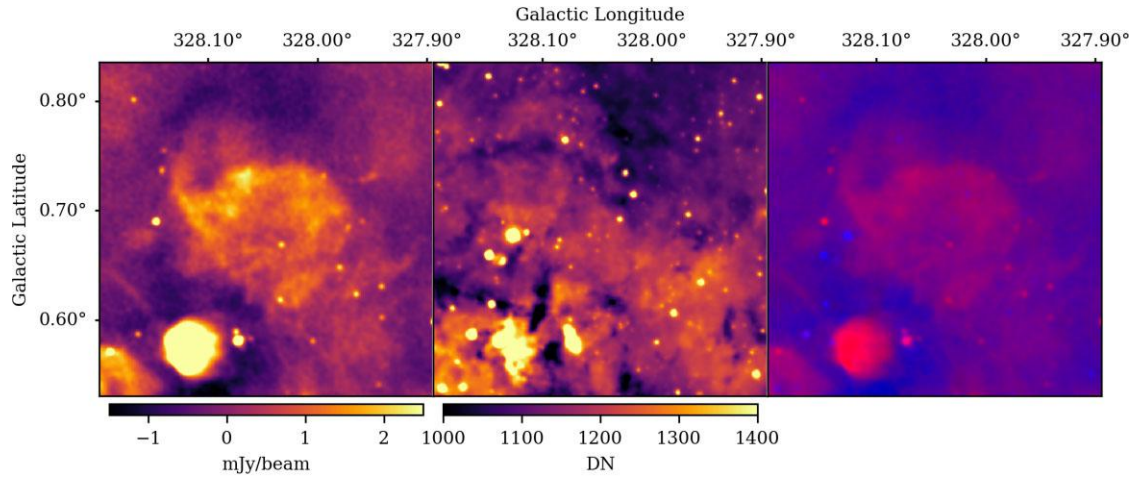


Figure B17. G328.0 + 0.7.

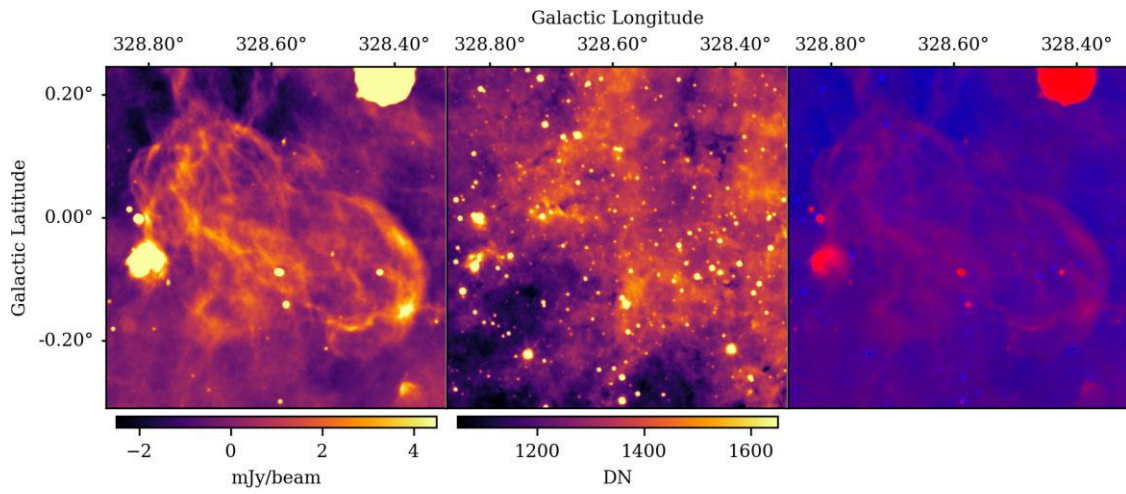


Figure B18. G328.6 + 0.0.

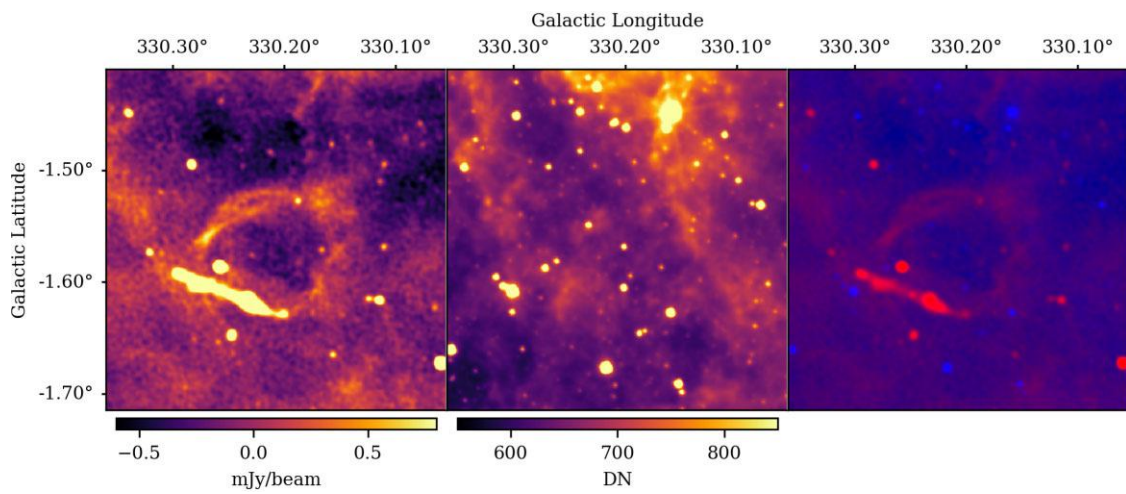


Figure B19. G330.2 - 1.6.

This paper has been typeset from a  $\text{\TeX}/\text{\LaTeX}$  file prepared by the author.